UNIVERSITY OF LATVIA
FACULTY OF PHYSICS AND MATHEMATICS

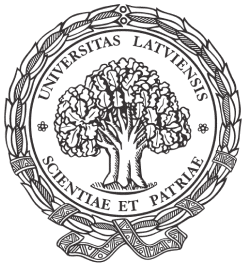

Dmitry Bocharov

FIRST PRINCIPLES SIMULATIONS ON SURFACE PROPERTIES AND REACTIVITY OF SUSTAINABLE NITRIDE NUCLEAR FUELS

Summary of Doctoral Thesis

Promotion to the Degree of Doctor of Physics
Subbranch: Solid State Physics

Scientific advisor: Dr. Chem. Yuri Zhukovskii

Riga 2012

This work was performed at the Institute of Solid State Physics, University of Latvia, beginning with October 2006 until August 2011.

Type of thesis: scientific papers

This work has been supported by the European Social Fund within the project „Datorzinātnes pielietojumi un tās saiknes ar kvantu fiziku" (Employment of computer sciences and its connection with quantum physics)
Līguma Nr. 2009/0216/1DP/1.1.1.2.0/09/APIA/VIAA/044

Scientific advisor: *Dr. Chem.* **Yuri Zhukovskii,** Senior Researcher, Institute of Solid State Physics, University of Latvia.

Reviewers of
Doctoral Thesis:

Dr. Lecturer **Girts Barinovs,** University of Latvia, Faculty of Physics and Mathematics.

Dr. Prof. **Roberto Caciuffo,** Institute for Transuranium Elements, Joint Research Centre, European Commission.

Dr. habil. Leading Researcher **Linards Skuja,** Institute of Solid State Physics, University of Latvia.

The defense of these Doctoral Thesis will take place in open session of the Physics, Astronomy and Mechanics Promotion Council of the University of Latvia to be held on January 24, 2012 at 15:00 in conference room of the Institute of Solid State Physics at Kengaraga Street 8, Riga, Latvia.

The full text of Thesis and its summary are available at Library of the University of Latvia (Kalpaka Blvd. 4, Riga, Latvia) and at the Latvian Academic Library (Rupniecibas Str. 10, Riga, Latvia).

LU Physics, Astronomy and Mechanics chairperson of Specialized Promotion Council: *Dr. Habil. Phys*., **Ivars Tāle**

ISBN 978-9984-45-437-5

Contents

Abstract

The uranium mononitride UN is a material considered as promising candidate for Generation-IV nuclear reactors. Due to considerable amount of aggressive oxygen impurities in UN samples, it is necessary to understand the mechanism of O adsorption and further oxidation of UN.

The first detailed study of UN surface, including its interaction with oxygen, have been performed using DFT PAW method as implemented in the *VASP* computer code. The formation energies of U and N vacancies as well as binding energies of O atoms and molecules adsorbed atop the UN surface are discussed together with the charge redistributions, densities of states, and O atom migration trajectories. Calculations allow us to propose energetically feasible mechanism for the partial saturation of UN(001) surface by oxygen which can lead to easy UN oxidation observed in air.

Keywords: Quantum chemistry, Density Functional Theory calculations, uranium mononitride, surface defects, oxygen adsorption

List of abbreviations

2D: Two-dimensional

3D: Three-dimensional

AE: All-electron

AFM: Antiferromagnetic state

BS: Basis set

BZ: Brillouin zone

CASTEP: Commercial and academic software package within formalism of PW and pseudopotentials

CRYSTAL: General-purpose computer code for *ab initio* LCAO study of periodic systems and molecules

DC: Direct current

DFT: Density functional theory

DOS: Density of states

EC FP-7: Seventh Framework Programme of the European Commission

EXAFS: Extended X-ray absorption fine structure

fcc: face centered cubic structure

FM: Ferromagnetic state

GAUSSIAN: General-purpose computer code, to enable *ab initio* LCAO electronic structure calculations

GGA: Generalized gradient approximation

ISSP: Institute of Solid State Physics, University of Latvia

KKR-GF: Korringa-Kohn-Rostoker Green's function

LAPW: Linearized augmented-plane wave

LC: Large core pseudopotentials

LCAO: Linear combination of atomic orbitals

LDA: Local density approximation

LMTO: Linear muffin-tin orbitals

ML: Monolayer

MT60: Mosyagin-Titov's small-core pseudopotential for atom containing 60 electrons in core

MT78: Mosyagin-Titov's large-core pseudopotential for atom containing 78 electrons in core

PAW: Projector augmented-waves

PBE: Perdew-Burke-Ernzerhof exchange-correlation functional-

ppm: particles *per* million

PS: Pseudo-wave soft function

PW: Plane waves

PW91: Perdew-Wang-91 exchange-correlation functional

RBS: Rutherford backscattering spectroscopy

RECP: Relativistic effective core pseudopotetntial

RMM-DIIS: Residual minimization method in the direct inversion of iterative subspace

SC: Small core pseudopotentials

SC60: Stuttgart-Cologne group pseudopotential for atom containing 60 electrons in core

SEM: Scanning electron microscopy

UPS: Ultraviolet photoelectron spectroscopy

US-PP: Ultra-soft pseudopotential

UV: Ultra-violet

VASP: Vienna *ab initio* simulation package within formalism of PW and pseudopotentials

wt%: weight percents

XPS: X-ray photoelectron spectroscopy

XRD: X-ray diffraction

1. Introduction

1.1. Motivation

Uranium mononitride (UN) is an advanced material for the non-oxide nuclear fuel considered as a promising candidate for the use in Generation-IV fast nuclear reactors to be in operation for the next 20-30 years [1, 2]. UN reveals several advantages over a traditional UO_2–type fuel (*e.g.*, higher thermal conductivity and metal density as well as high solubility in nitric acid in the case of fuel reprocessing [2]). However, one of important problems with actinide nitrides is their effective oxidation in oxygen-containing atmosphere (even at low partial pressure) which can affect nuclear fuel performance [3, 4]. Thus, it is important to understand the mechanism of the initial stage of UN oxidation and to find proper solutions, in order ways to improve the quality of nuclear fuel in the future.

The main objective of this PhD Thesis is to acquire reliable information on the atomic and electronic structure of both perfect and defective UN surfaces as well as to understand the mechanism of early stages of surface oxidation. This must be achieved through the solution of the following tasks:

- Modeling of an UN bulk for proper choice of parameters for surface calculations.
- Modeling of perfect UN surface with a focus on the surface anisotropic relaxation and reconstruction.
- Modeling of single N and U vacancies and calculations on formation energies of surface defects.
- Modeling of both molecular and atomic oxygen adsorption upon perfect UN surfaces.
- Modeling of oxygen migration upon both perfect and defective UN (001) surface.
- Modeling of O adatom incorporation inside existing surface vacancy.
- Comparison of results obtained for UN (001) and (110) surfaces.
- Development of an atomistic model for oxidation of UN surface.

The current study is performed within the collaboration between Institute of Solid State Physics, Riga, and Institute for Transuranium Elements, Karlsruhe, Germany, (Contract No 205343-2006-07 F1ED KAR LV) and as one of tasks included in the EC FP-7 project: Basic Research for Innovative Fuel Design for Generation-IV systems (F-BRIDGE).

1.2. Author's contribution

Main results of our calculations considered and analyzed in this PhD Thesis were described in 5 papers published in high-ranking International scientific journals [P1-P5] as well as presented at International and Local conferences as posters and oral reports (see conference list in Section 13). The author substantially contributed to preparation and

writing of papers and conference presentations, he was also selected as the corresponding author for Refs. [P2-P5].

Major part of considered results were obtained by author using PW calculations (*VASP* code) (almost all calculations presented in the papers [P1-P5] excluding calculations on N_2 molecule and alpha-uranium crystal [P4, P5]), although LCAO calculations (*CRYSTAL* code) were performed too [P1, P2] (in cooperation with St. Petersburg State University, Russia), to compare both *ab initio* approaches used for simulations on UN substrate and its chemical reactivity. The author installed computer codes in single and parallel regime at both Latvian Supercluster (LASC, ISSP, Riga) and Computational Facilities of Research Center Garching (Germany). Moreover, the author optimized both input parameters and key sets for *VASP* code (see Section 3 for details), performed careful analysis of output files and extracted results for further treatment and interpretation, as well as wrote several scripts, to operate this code and to perform analysis of obtained results (for example, to plot DOS from *VASP* output file, to construct bulk structure, to calculate magnetic moments and bulk modulus as well as to distribute resources in parallel calculations).

Due to a restricted number of theoretical and experimental data available in literature so far, very important question was a proper verification of the calculated results presented in this PhD Thesis. The author chose the following verification methods:

1. *Comparison of obtained results with existing experimental or theoretical data.*

For example, as known from literature [1], the UN lattice constant $a_0 = 4.886$ Å, the bulk modulus $B = 194$ GPa and the cohesive energy $E_0 = 13.6$ eV. These parameters were used for comparison with values obtained in theoretical calculations performed in this study.

2. *Simultaneous application and comparision of different theoretical methods.*

The results of our PW calculations on UN bulk and perfect (001) surface as well as atomic oxygen adsorption on this substrate were compared with the corresponding LCAO results calculated by group of Prof. R.A. Evarestov (*St. Petersburg State University*) [P1, P2]. Qualitative accordance of results obtained using the two different first-principles methods greatly increases the reliability of obtained results.

3. *Finding of internal criteria for convergence.*

For example, in calculations on vacancy-containing UN slab, the control of spin distribution is very important. Averaged magnetic moment μ_{av} *per* U atom in spin-relaxed calculations must be larger than 1 μ_B, otherwise we cannot achieve a convergence of formation energies for defects depending on thickness of UN slab [P4]. This effect appears due to a presence of local energy minima for considered slab configurations. Global energy minimum corresponds to spin redistribution with $\mu_{av} > 1$, while for other redistributions, we failed in localization of global minima, *i.e.*, reliability of obtained results is rather doubtful.

4. *Comparison of results obtained for the same system with varied computational parameters.*

For example, we compared vacancy formation energy for the same defect periodicity (2×2 or 3×3) but for different number of atomic layers; we also found criteria for cut-off energy divergence (see Section 3 for details) [P4].

1.3. Scientific novelty

Theoretical simulations of uranium compounds are especially complicated due to a relativistic character of an electron motion inside the U atomic core. Moreover, UN is characterized by a mixed metal-covalent chemical bonding: physical and chemical properties of light actinides are determined by partly localized *5f* electrons, requiring time-consuming calculations. In this study, we *firstly* present DFT calculations on UN surface and propose the UN surface oxidation mechanism. These results convincingly illustrate possibilities of quantum-chemistry simulations on actinides and their surfaces. Obtained results can be used for verification of alternative theoretical calculations on uranium nitrides and related actinide compounds (for example, uranium monocarbide UC). Moreover, the results of DOS analysis presented in this work can be used for qualitative interpretation of the experimental ultra-violet photoelectron spectra (UPS) for uranium oxynitrides which will be synthesized in the future.

2. Literature review

2.1. Experimental study of UN properties

Uranium mononitride is a compound with metallic lustre and low electrical resistivity ($1.6 \cdot 10^{-4}$ cm) [5], possessing *fcc* structure (space group $Fm\bar{3}m$, Fig. 2.1) over a wide temperature range [1]. The UN lattice constant is sensitive to carbon impurities [1] being insensitive to small oxygen impurities [6]. High melting point (~2780±25 K) [1], high fissile atom density (14.32 g/cm^2 vs 10.96 g/cm^2 for UO_2 [7]) and high thermal conductivity (13 W/mK) [8] make UN fuel a prospective material for nuclear reactors [1].

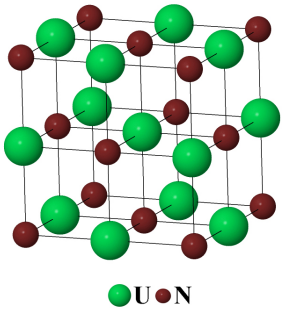

Figure 2.1. *fcc* structure of uranium mononitride

Various fabrication methods were used so far to produce UN. Samples of uranium nitrides were produced beginning with 19th century by annealing either UCl_4 salt in NH_3 atmosphere or uranium bicarbide (UC_2) in nitrogen at 1100 °C [1]. Nowadays, the most widespread UN fabrication methods are:

- Nitration of uranium in N_2 or NH_3 atmosphere at ~800-900 °C. Frequently, U_2N_3 is used as an intermediate product which subsequently is decomposed, to obtain UN powder with a low concentration of oxygen impurity [1].
- Carbothermic reduction. Formation of UN in the carbothermic reduction/nitrification process is possible, starting with pressed mixtures of UO_2 + C, following the reaction $UO_2 + 2C + 1/2N_2 \rightarrow UN + 2CO$ that are held at 1700 °C in N_2, N_2/H_2 or NH_3 atmosphere. However, such products contain a large amount of O_2, typically 0.1 wt% [1, 9].
- Nitration of melting U in N_2 gas by voltaic arc at pressure of 3-5 bar. If tungsten electrodes are used, a pollution of resulting UN material with W impurities is unavoidable. This is why U electrodes at higher N_2 pressure (20 bar) were also used [1]. The products, however, are also inhomogeneous.
- Hydride route. This method results in formation of a good quality powder with particle size ~1 μm. When using such a method, UH_3 is produced by reacting U

with H_2 at 200-300 °C. It is subsequently decomposed ($UH_3 \rightarrow U + 3/2H_2$) to a U powder in inert gas atmosphere or in vacuo at temperature 400-600 °C. U powder reacts with N_2 at 800 °C, to yield UN_{1+x}, which can be decomposed to UN, as above, by heating at temperatures between 1100 and 1300 °C in vacuo. A direct reaction between UH_3 and N_2 was used too [1].

- Alternative processes of UN fabrication, starting with the halides UF_4 or $UC1_4$, are less important for commercial production [1]. Notice, that for scientific researches, just specific alternative methods are frequently used. For example, UN surface could also be produced by bombardment of an U metal surface by activated nitrogen [10].

Fascinating and often enigmatic array of UN magnetic and electronic properties is induced by U(5*f*) electrons which are found to be intermediate between the highly localized 4*f* electrons of the lanthanides and the strongly delocalized *d* valence electrons in the transition metals [11]. The UN was found to be antiferromagnetic at temperatures lower than a Neel temperature (T_N ~ 53 K), which was detected in the heat capacity measurements [1]. Investigation of the magnetic structure of uranium nitride was performed in 60s using methods of neutron diffraction [5]. The magnetic structure known as ordering of the first kind, where ferromagnetic sheets parallel to the (001) planes are antiferromagnetically coupled, was deducted [5]. The value of 0.75 μ_B found for the magnetic moment at low temperatures appears to be surprisingly small (the lowest amongst the uranium monopnictides UX, where X = P, As, Sb) [5] which requires a careful analysis of results for UN surface obtained using the DFT calculations and their comparison with the corresponding experimental data.

Photoelectron spectroscopy also confirmed the complexity of UN. A very high density of states in proximity of the Fermi level was observed, which gives an evidence that the U(5*f*) electrons participate in bonding being strongly hybridized with the U(6*d*) electrons. The occupation of the conduction U(5*f*) band is 2.2 ± 0.5 *e*, of which ~1.8 *e* resides near the Fermi level [11]. In [12], the band structure of UN at 25 K was constructed taking into account the second derivative of high-resolution angle-resolved photoemission spectra. A highly dispersive band was observed for UN near the Fermi level centered at Γ(X) point, whose bottom is located at about 2 eV. First magneto-optical Kerr measurements on UN also shows narrow U(5*f*) band formation around the Fermi level as well as increased hybridization of the U(5*f*) states with U(6*d*) and N(2*p*) states as compared to similar data for heavier uranium monopnictides [13]. On the other hand, uranium nitride has the smallest U-U distance amongst the UX compounds (X=N, P, As, Sb, S, Se, and Te) which is equal to 3.46 Å being close to the critical 3.4 Å value given by Hill diagrams separating non-magnetic from magnetic compounds, so that delocalization of U(5*f*) states should be expected [14].

Extraction of the data for diffusion of nitride atoms or vacancies is also non-trivial for UN. Unfortunately, a radioactive isotope suitable for diffusion measurements does not exist for nitrogen. Therefore, either mass-spectrometric measurements with ^{15}N or a nuclear reaction induced in the UN specimen following the annealing are needed, to measure nitrogen diffusion coefficients [1]. On the other hand, thermally created and radiation-induced point defects can be studied by measuring a physical quantity sensitive to their presence. For example, the electrical resistivity ρ for actinide compounds can be

used for this purpose: the changes of ρ depending on vacancy concentration are found to be very large (for example, 12 μΩ·cm for 1% of C vacancies in UC) [1]. By studying the thermal recovery of these defects during isochronal annealing, or also by applying the "change-of-slope method" during isothermal annealing with suddenly increased temperature, the defect migration energy can be determined. Unfortunately, these methods do not identify the defect or even the type of atom involved (*e.g.,* C, O or N), unlike the diffusion studies with radioactive tracers [1].

2.2. Interaction of uranium nitride with oxygen

Initially, the oxidation of uranium mononitride in an oxygen atmosphere was systematically studied in [15]. The two main types of UN samples were used for those experiments: powdered UN and smoothly polished UN pieces. Following a weight change of the UN powder sample during the oxidation process at elevated temperatures, a strong exothermic reaction was identified at 250 °C characterized by rapid oxygen absorption. The weight was increased by 11.5%. X-ray diffraction patterns of the intermediate product at temperatures 250-260 °C showed both weak diffraction lines corresponding to UN and very pronounced line broadening corresponding to UO_2. Smoothly polished UN pieces were used for kinetic study of UN oxidation. Measurements showed that reaction rate is proportional to the area covered by the oxide or the oxidized volume. Analysis of both kinetic studies and X-ray diffraction data suggested that the isothermal oxidation of UN proceeds from the beginning of lateral spreading of the oxide, $UO_2(N)$, accompanied by a slight N_2 release and by the formation of $U_2N_3(O)$ during the reaction between UN and released nitrogen.

In [16], such characteristics as the chemical composition, phases, lattice parameter, sinterability, grain growth and thermal conductivity of the samples are investigated using chemical, X-ray and ceramographic analyses for pellets of uranium nitride powder containing certain amounts of oxygen (~0.3, ~0.6 and ~1.0 wt%) which are products of carbothermic reduction. Note, that conductivity of UN samples was found to be gradually decreased under oxidation [16]. The principal results are that the average UN grain size of matrix phase decreases with increase of oxygen content. Moreover, thermal conductivity of the pellets containing about 1 wt% oxygen is lower than that of usual nitride pellets (containing 1000-2000 ppm oxygen) by 9-10% and 12-13% at 1000 and 1500 K, respectively.

In [9], direct ammonolysis of UF_4 was used, to synthesize UN_2 sample which was heated to 1100 °C for 30 min inside the inert atmosphere producing these UN powder samples with UO_2 inclusions saturated at 5.0 wt%. The methods of X-ray diffraction (XRD) and scanning electronic microscopy (SEM) were used for morphology analysis of these samples. The SEM images show that UN particles are primarily irregular grains with incompletely crystallized faces (Fig. 2.2). The observed characteristic length distribution of particles ranges from 0.1 to 6 μm. The measured UN surface area was equal to 0.23 m^2/g. Both the electron microprobes and X-ray diffraction analysis showed that there are considerable amount of oxygen impurities in UN samples consisting of the primary UN phase and the secondary UO_2 impurity phase. This supports the conclusion that oxide impurities are likely to be formed by a diffusive process from the chemical environment

and, thus, they are also likely to be formed along the particle surface. Concentration of oxygen impurities increases upon exposure to air: UN sample exposed for 3 months shows the growth of oxide contamination. The quantitative analysis performed for the XRD patterns showed that the UO_2 concentration increases from 5.0 wt% to 14.8 wt% over this time period [9].

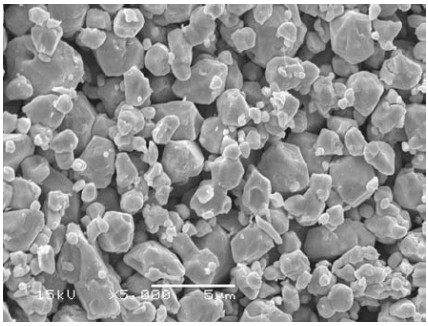

Figure 2.2. SEM image of UN sample [9].

UPS measurements performed for thin layers of UO_2, UN, UO_xN_y and UO_xC_y using He-II 40.81 eV excitation radiation produced by a UV rare-gas discharge source were described in [17, 18]. These layers were prepared *in situ* by reactive DC sputtering in an Ar atmosphere. Fig. 2.3 shows that U(5*f*) states form a peak close to the Fermi level (0 eV), which proves their itinerant character. The valence band spectrum of UO_xN_y shows a broad band interpreted as superposition of the narrow O(2*p*) and N(2*p*) bands. The maximum at 6 eV binding energy clearly comes from the O(2*p*) state contribution while the smaller shoulder at 3 eV coincides with the N(2*p*) signal in UN sample.

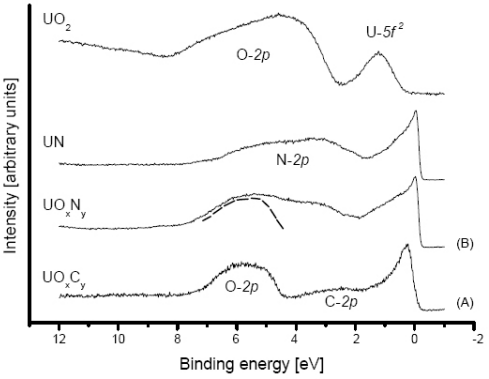

Figure 2.3. He-II valence band spectra of UO_xC_y, UO_xN_y, UN and UO_2 spectra are given as reference [18].

In [19], XPS and XRD methods as well as the measurement of ammonia concentration in the aqueous phase at the end of each experiment were used, in order to study corrosion of UN in water. UO_2 film arising during the surface reaction with water was detected using XPS for the surface of freshly polished UN pellet. The high corrosion rates of UN in water (at 928 °C) indicated that UN is not stable inside the hot aqueous environment. Corrosion rate for UN is much lower than that for U metal but higher that of uranium silicide.

Thickness, composition, concentration depth profile and ion irradiation effects on uranium nitride thin films deposited upon fused silica were investigated in [8] using Rutherford Backscattering Spectroscopy (RBS) for 2 MeV He^+ ions. Deposition at -200 °C provided formation of thick stoichiometric UN film. This film was found to be stable for exposure to air. The surface oxidation is much more enhanced and the oxidized surface layer becomes gradually thicker in films deposited at higher temperature (+25 °C and +300 °C). A large influence of the ion irradiation on the film structure and layer composition was observed. This study also showed possibility to produce stoichiometric UN film with the required uranium content of 50% and to obtain the required film thickness by ion irradiation.

Finally, experimental studies also clearly showed that oxygen contacting to the surface of uranium mononitride can result in growth of the oxide compound and, at initial stages, can lead to the formation of surface layer structurally similar to oxynitrides UO_xN_y [14].

2.3. Previous theoretical simulations on UN and related actinide compounds

Due to increasing interest to the fast breeder reactors and to the issues of transmutation of uranium, plutonium and minor actinides, first-principles and other theoretical calculations on actinide nitride compounds attract great attention nowadays. However, previous theoretical studies were performed mainly on UN bulk. Beginning with 80s [21-23], for its *ab initio* calculations, the methods based on the DFT were mainly used.

In first relativistic calculations on UN single crystal, there were used methods of full-potential Korringa-Kohn-Rostoker (KKR) Green's function [21] and Linear Muffin-Tin Orbitals (LMTO) [22, 23] focused mainly on the atomic and electronic structure. The calculated lattice parameters were found within 3% of experimental value, whereas the bulk modulus was reproduced worse when comparing with experimental data: by 23% higher [22] or within 10% [23]. DOS analysis showed that no gap exists between the valence and conduction bands in UN. The valence bands, found to be ~5-6 eV wide, appeared below the Fermi level by ~2 eV. The main peak was located below the Fermi level by 1 eV [23].

Recently, a number of first-principles DFT calculations on UN bulk were performed. In particular, the all-electron calculations within the Linear Augmented Plane Wave (LAPW) approach were performed, using the PBE (Perdew-Burke-Ernzerhof) exchange-correlation functionals (with and without incorporation of the spin-orbital coupling) as implemented in the *WIEN-2k* program package, for a series of actinide nitrides

(AcN, ThN, PaN, UN, NpN, PuN, AmN) [20]. The enthalpies of their formation, which main contribution arises from the ground state cohesive energies, were evaluated. The obtained enthalpies of formation were found to be in excellent agreement with the experimental data (in the case UN, the best correlation was achieved with results of calorimetric measurements: theoretical value of -291.0 kJ·mol^{-1} *vs.* experimental value of -290.5±1.4 kJ·mol^{-1} [24]). Certain discrepancies with experimental data observed for PuN and ThN still need to be clarified.

In [25], the same LAPW formalism within the GGA approximation was used to study the structural, electronic, and magnetic properties of the actinide compounds. The observed chemical bonding between the actinides and nitrogen was characterized by a significant ionic character. The calculated cohesive energies were found to be close to the experimental values (14.3 eV *vs.* 13.6 eV, respectively). Although lattice constants were calculated in a good agreement with the experiment (within ~0.4%), the UN, AmN, PuN, and NpN were found to be ferromagnetic (FM) that contradict to experimental results for these compounds (antiferromagnetic structures were experimentally observed at low temperatures). The calculated spin density for UN in FM state was equal to 0.96 μ_B. On the other hand, the calculated ferromagnetic structure of NpN and the non-magnetic structure of ThN agreed well with the corresponding experimental measurements.

In [26], the all-electron relativistic spin-polarized DFT calculations were performed, to evaluate the total energies, optimized geometries, as well as electronic and thermodynamic properties of perfect stoichiometric UN and UN_2 single crystals. For this purpose, the GGA PW91 exchange-correlation functional was used, and the numerical double-ξ basis sets with *d*-type polarization functions were added to atoms heavier than hydrogen. Structural properties recently measured using EXAFS and XRD methods were successfully reproduced in theoretical calculations (within error of 0.03 Å). Calculated DOSs showed hybridization of the U(*6d*), U(*5f*) and N(*2p*) states as well as domination of the U(*5f*) state in the conduction band. Novelty of that paper consisted in a calculation of the phonon frequencies and heat capacities. The authors suggested an important role of itinerant U(*5f*) states in thermodynamic properties.

The lattice parameters, electronic structure, as well as the thermodynamic properties of UN using LDA+*U* and GGA+*U* semi-empirical schemes included Hubbard potential *U* were presented in [27]. The total energy dependences on *U*-parameter for UN bulk in FM and AFM states obtained in those calculations show that FM state is preferable for the range of *U*-parameter between 0 and 2 eV while AFM state could be favorable for *U*-parameter larger than 2 eV. Nevertheless, even though the AFM state of UN bulk is reproduced, the ground state in hardly obtainable when using the DFT+*U* method [28]. This may produce large errors when calculating defect formation energies [29, 30]. We avoid application of this method in the present study due to ferromagnetic nature of UN surface [31], reproducible by standart DFT functionals.

The PW approach was applied for UN atomic structure calculations beginning with [32]. In that study, where the Ultra-Soft (US) pseudopotentials and PBE exchange-correlation functional were used, the experimental UN and U_2N_3 lattice constants were reproduced within 3% error while the difference of their atomic coordination can be described within 5% error.

In more detailed PW calculations on UN bulk, the *VASP* and *CASTEP* codes were employed using the Perdew-Wang (PW91) non-local GGA exchange-correlation functional combined with either US or PAW pseudopotentials, respectively [33, 34]. Both series of calculations agree well on the mixed metallic-covalent nature of UN chemical bonds qualitatively reproducing the lattice constants, bulk moduli and cohesive energies.

Then the PW approach combined with a supercell model was used for the calculations on defective UN crystal, containing single point defects as well as Frenkel and Schottky defect pairs. In [34], it was shown that N vacancies practically have no influence on the UN lattice constant, even for concentrations higher than 25%. The formation energies of U or N vacancy in UN bulk were obtained equal to 9.1-9.7 eV for N vacancy and 9.4-10.3 for U vacancy. The calculated activation energy of the interstitial N atom migration along the (001) axis was estimated as rather low, 2.73 eV [33]. This fact confirms the suggestion that the interstitial migration might be a predominant mechanism of N diffusion in UN fuel [1]. Apart the behavior of empty vacancies, the O atom incorporation into vacancies in bulk UN was considered too [35]. Its incorporation into the N vacancies was found to be energetically more favorable as compared to the interstitial sites. However, the calculated values of solution energy showed an opposite effect. The calculated migration energy of the interstitial O atoms is very similar (2.84 eV). This fact confirms that O atoms can easily substitute the host N atoms in UN structure.

Recent LCAO calculations on UN bulk [36, 37] were performed using the *GAUSSIAN-03* computer code with the PW91 exchange-correlation functional. The values of cohesive energy calculated using the Relativistic Effective Core Potentials RECP78 and RECP60 considerably differ (9.86 eV and 12.8 eV, respectively), thus indicating an importance of variation for the U outer shell. Group-theoretical analysis performed for interpretation of the UN band structure showed that both the bottom of the conducting band and the top of the valence band are formed by U(*5f*) states which result in the metallic nature of UN [36, 37] unlike UO_2 which is a semiconductor [38]. The Mulliken effective atomic charges of ±(1.5-2.0) *e* calculated using the *GAUSSIAN-03* code confirmed the mixed nature of the UN chemical bonding, being in agreement with the Bader topological charges of ±1.6 *e* obtained in PW calculations [34].

A number of studies on related actinide compounds were also published in last years. In [29], formation energies of oxygen vacancy in UO_2 compound were calculated using the Dudarev's DFT+*U* approach [39]. The formation energy of oxygen vacancy in UO_2 bulk was found to be 3.5-5.67 eV. In [40], formation energies of O and U vacancies were calculated using GGA approximation. Those calculations showed small difference between the FM and AFM states (4.0 eV for U vacancy formation in FM state *vs.* 4.4 eV for AFM state as well as 6.1 eV in both cases for O vacancy). In [41], point defects in uranium monocarbide bulk were studied using the PAW method combined with the PBE functional. The formation energy of uranium vacancy was found to be 4.54-4.55 eV while the same energy for carbon vacancy was equal to 0.8-0.83 eV. The mechanical properties of NpN were studied using the same GGA PBE functional [42]. The calculated bulk modulus for NpN ranged within interval 147-227 GPa depending on the magnetic state (AFM, FM or non-magnetic).

The first electronic structure simulations on actinide surfaces and their reactivity towards the molecular and atomic oxygen were performed only recently. It is, however, not surprising since actinide surfaces cannot be easily calculated using the DFT methods, due to a large number of electrons *per* unit cell. Nevertheless, some results on simulations performed for α-U, δ-Pu and UO_2 surfaces are available in the literature. In particular, Taylor [43] showed that the PAW method [44], used also in the present study, is fitting for reliable calculations on the (001) surface of α-U.

Tan *et al.* obtained UO_2 surface energies, using the atomic-scale computer simulation within the approach of interatomic potentials, which systematically classifies the 153 unique planar surface configurations that can be generated within 2×2 supercells [45]. The calculated surface energies ranged between 2.28 and 3.12 eV for UO_2(001) surface and 1.27-1.54 eV for UO_2(111) surface. The PW91 functional has been used for simulations on (111), (110), and (100) surfaces of UO_2 [46]. The calculations showed that the (111) surface has the lowest surface energy (0.461 J/m^2), followed by the (110) surface (0.846 J/m^2), and the (100) surface (1.194 J/m^2).

The calculations performed by Atta-Fynn and Ray [47, 48] also confirm the effectiveness of DFT methods for calculations on O, C and N ion chemisorption upon the δ-Pu(111) surface. The calculations were performed using the GGA PBE exchange-correlation functional. A 50% surface coverage by adatoms was considered. Calculations were performed at two levels: with and without spin-orbit coupling. Inclusion of spin-orbit coupling lowers the chemisorption energy by 0.05–0.27 eV, on the other hand, it negligibly influences on chemisorption geometries. Analysis of effective charges for each atom indicates that chemisorption primarily occurs on the surface layer. Pu-adatom hybridizations is dominated by Pu(6*d*) and adatom 2*p* states, with a significant reduction in the first peak of the projected Pu(5*f*) DOS, indicating the delocalization of some Pu(5*f*) electrons.

In any case, for the moment, no results of UN surface calculations are found to be published in the literature, excluding the current study performed within this PhD Thesis [P1-P5].

3. Theoretical background

For UN modeling, we use the *VASP-4* computer code, the commercial complex package based on density functional theory (DFT) and included an iterative solution of Kohn-Sham equations, based on residuum-minimization and optimized charge-density mixing routines [49], employing a plane-wave basis set combined with either US or PAW pseudopotentials. Elaboration of *VASP* package was began at early 90s.

3.1. DFT method basics

The cornerstone of DFT was laid by Hohenberg–Kohn (HK) theorem, which suggests that ground state properties of a many-electron system should be uniquely determined by an electron density $\rho(\vec{\mathbf{r}}) = \rho(\vec{\mathbf{r}}, \vec{\mathbf{r}}')$. The total energy of system in this case can be written as

$$E(\rho(\vec{\mathbf{r}})) = \int V(\vec{\mathbf{r}})\rho(\vec{\mathbf{r}})d\vec{\mathbf{r}} + T[\rho(\vec{\mathbf{r}})] + \frac{1}{2}\int \frac{\rho(\vec{\mathbf{r}}')\rho(\vec{\mathbf{r}})}{|\vec{\mathbf{r}} - \vec{\mathbf{r}}'|} d\vec{\mathbf{r}}' d\vec{\mathbf{r}} + E_{xc}[\rho(\vec{\mathbf{r}})], \qquad \textit{(Eq. 3.1.1)}$$

where the first term on right hand side describes the external potential influencing on the interacting system, for example, attraction of electrons to atomic nucleus, the second term describes the kinetic energy of electrons, the third term denotes the so-called Hartree term describing the electron–electron Coulomb repulsion, while the last term is called the exchange-correlation potential and includes all other contributions, in particularly the many-electron interactions [50, 51].

Varying the full energy functional (*Eq. 3.1.1)*, the Kohn-Sham one-electron equations (similar to Hartri-Fock equations) may be derived:

$$(\hat{\mathbf{H}} + \hat{\mathbf{J}} - \hat{\mathbf{V}}_{xc})\varphi_i(\vec{\mathbf{r}}) = \varepsilon_i \varphi_i(\vec{\mathbf{r}}), \qquad \textit{(Eq. 3.1.2)}$$

where the term $\hat{\mathbf{V}}_{XC}[\rho(\vec{\mathbf{r}})] = \frac{\delta E_{xc}[\rho(\vec{\mathbf{r}})]}{\delta\rho(\vec{\mathbf{r}})}$ is the exchange-correlation potential [50].

Due to dependence of Hamilton and Coulomb operators $\hat{\mathbf{H}}$ and $\hat{\mathbf{J}}$ in Kohn-Sham equations on electronic density $\rho(\vec{\mathbf{r}})$, these equations should be solved using self-consistence method [50].

Contemporary DFT calculations on solids are determined by several key options: (*i*) the choice of exchange-correlation functional, (*ii*) the choice of a basis set to expand the Kohn-Sham eigenfunctions (plane waves or localized basis functions), and (*iii*) the choice of a way to describe interactions between the ionic core and the valence electrons (full-potential approach or pseudopotential approach) [52].

3.2. Exchange-correlation functionals

Since the exact form of exchange-correlation functional is not known, tremendous progress in quantum chemistry methods is achieved by creation of proper functionals. Functionals of different complexity were developed within the hierarchy of DFT

functionals. The simplest approximation is the local-density approximation (LDA) based on the exact exchange energy for a uniform electron gas which can be obtained from fits to the correlation energy for a uniform electron gas [50].

In the present study, we use the Generalized Gradient Approximation (GGA) functionals, which foresee that the electronic density is unevenly distributed: the highest density of electronic density is located around the atom nucleus. The exchange-correlation energy may be expanded in the Taylor Series depending on the electronic density degrees. If only the first order of expansion is taken into account the resulting expression contains an electronic density gradient $\nabla\rho$ [50, 53].

Real functional is typically formed involving the fitting parameters which can reproduce the experimental data for different classes of materials with a high accuracy. It is very important to find such a functional, which can be used for description of large number of systems without additional parameters involved during calculation (In this sense, such calculations are called as *ab initio* or first principles calculations). In our study, the PW91 exchange-correlation functional has been used [54].

3.3. The pseudopotentials

Formalism of the pseudopotentials uses the widespread quantum-chemical approaches: the chemical properties are mostly determined by the valence electrons, the inner shells are chemically rather inert, while shells half-filled or completely filled with electrons possess the spherical symmetry (so-called Unsold's Theorem [55]). It allows us to describe separately only the outer shells' electrons. In turn, all inner electrons can be substituted by a joint effective pseudopotential. Depending on number of included electrons the pseudopotentials can be separated as Large Core (LC) and Small Core (SC) RECP pseudopotentials.

For example, U atom possesses the $1s^2 2s^2 2p^6 3s^2 3p^6 3d^{10} 4s^2 4p^6 4d^{10} 4f^{14} 5s^2 5p^6 5d^{10} 6s^2 6p^6 7s^2 5f^3 6d^1$ electronic structure. The LC(U) potential includes 78-electron core potential ($[Xe]4f^{14}5d^{10}$) and 14 valence electrons ($6s^2 6p^6 7s^2 5f^3 6d^1$) while the SC(U) potential includes 60-electron core potential ($[Kr]4d^{10}4f^{14}$) and 32 valence electrons ($5s^2 5p^6 5d^{10} 6s^2 6p^6 7s^2 5f^3 6d^1$). Unlike the LCAO RECP pseudopotentials applied for *CRYSTAL* calculations, the RECP pseudopotentials for PW calculations cannot be directly re-optimized: creation of a new pseudopotential or its re-optimization is very complicated task requesting up to several months or years for its solution [56]. Main aim of the current PhD activity in respect to a proper applicaton of RECP pseudopotentials for reliable calculations is their optimal choice from the library of standard pseudopotentials supplying the *VASP* code (depending on both structure of the core and diference with the all-electron wave function). Choice of pseudopotential for the calculated system must be based on the character of bonding between the ions in the system [49] including its test calculations.

For calculations performed within the current PhD study, we have applied RECP pseudopotential for 78 U internal electrons (with $6s^2 6p^6 6d^2 5f^2 7s^2$ valence shell), as well as 2 core electrons for both N and O atoms (with $2s^2 2p^3$ and $2s^2 2p^4$ valence shells, respectively).

3.4. The plane wave formalism

The Kohn-Sham method employing a plane-wave basis set and the pseudopotential approximation is one of powerful techniques in contemporary computational material science. The use of a plane-wave basis has several immediate advantages [52]: (*i*) it is easy to change from a real-space representation (where the potential energy *V* has a diagonal representation) *via* a Fast Fourier Transform to momentum-space where the kinetic energy *T* is diagonal; (*ii*) the control of basis-set convergence is almost trivial; it is sufficient to monitor the eigenvalues and total energies as a function of the *cut-off* energy, *i.e.*, the highest kinetic energy of a plane-wave within the chosen basis set; (*iii*) the Hellmann-Feynman forces acting on the atoms and the stresses on the unit cell may be calculated straightforwardly in terms of the expectation value of the Hamiltonian with respect to the ionic coordinates; (*iv*) basis-set superposition errors that have to be carefully controlled in calculations based on local basis sets are avoided.

As a starting-point to solve Kohn-Shame equations in PW basis set, the Bloch theorem usually serves, which describes wave function of electron (or other particle) placed in a periodic potential [57], *i.e.*,

$$\psi_{n\mathbf{k}}(\mathbf{r}+\mathbf{R}) = \psi_{n\mathbf{k}}(\mathbf{r})e^{i\mathbf{kR}} \qquad \textit{(Eq. 3.4.1)}$$

The unit cell periodic part $u_{n\mathbf{k}}$ of the wave functions is introduced as

$$\psi_{n\mathbf{k}}(\mathbf{r}) = u_{n\mathbf{k}}(\mathbf{r})e^{i\mathbf{kr}}, \qquad \textit{(Eq. 3.4.2)}$$

where $u_{n\mathbf{k}}(\mathbf{R}+\mathbf{r}) = u_{n\mathbf{k}}(\mathbf{r})$. It means that all cell periodic functions can be written as a sum of plane waves, going to reciprocal space lattice and performing Fourier transform:

$u_{\mathbf{k}}(\mathbf{r}) = \sum_{\mathbf{G}} u_{\mathbf{k}}(\mathbf{G})\mathrm{e}^{i\mathbf{Gr}}$ ($\mathbf{G}$ is chosen by such a way that $\mathrm{e}^{i\mathbf{Gr}}$ has the periodicity of the real space lattice)

$$\psi_{\mathbf{k}}(\mathbf{r}) = (N\Omega_0)^{-1/2}\sum_{\mathbf{G}} u_{\mathbf{k}}(\mathbf{G})\mathrm{e}^{i(k+\mathbf{G})\mathbf{r}}, \qquad \textit{(Eq. 3.4.3)}$$

where $u_{\mathbf{k}}(\mathbf{G}) = \frac{1}{\Omega_0}\int_{\Omega_0} \mathrm{e}^{-i\mathbf{Gr}} u_{\mathbf{k}}(\mathbf{r})d\mathbf{r}$ (Fourier transform).

In fact, the number of plane waves can be determined as a function of the kinetic energy cut-off, thus forming the PW sphere $\frac{(\mathbf{k}+\mathbf{G})^2}{2} < E_{cut}$ in reciprocal space [57].

Development of PW formalism as used in *VASP* computer code resulted in implementation of the *projector-augmented wave* (PAW) *method* originally introduced by Blöchl [44]. The main idea of PAW method is to transform the physically relevant full all-electron (AE) Kohn-Sham wave functions Ψ_n of this Hilbert space into a new computationally convenient pseudo-wave soft (PS) variational functions $\tilde{\Psi}_n$ in so-called

pseudo-Hilbert space [58]. Within the PAW formalism the AE wave function is derived from the PS wave function by means of a linear transformation [44]:

$$|\Psi_n\rangle = |\tilde{\Psi}_n\rangle + \sum_i (|\varphi_i\rangle - |\tilde{\varphi}_i\rangle)\langle \tilde{p}_i | \tilde{\Psi}_n \rangle \qquad \textit{(Eq. 3.4.4)}$$

where the AE partial waves φ_i are obtained for a reference atom whereas the PS partial waves $\tilde{\varphi}_i$ are equivalent to the AE partial waves outside a core radius r_c^l and match continuously onto $\tilde{\varphi}_i$ inside the core radius (the augmentation region, similar to linearized muffin-tin LMTO formalism); the index i is a shorthand for the atomic site R_i, the angular momentum numbers $L = l, m$, and an additional index k referring to the one-electron reference energy ε_{kl}. The core radius is chosen approximately about half the nearest-neighbor distance [58]. The projector functions $\tilde{p}_i$ are dual to the PS partial waves:

$$\langle \tilde{p}_i | \tilde{\varphi}_j \rangle = \delta_{ij} \qquad \textit{(Eq. 3.4.5)}$$

3.5. Computational parameters in the *VASP-4* computer code

In previous subsections, we have desribed general theoretical principles which are included in *VASP* computer code. In this subsection we shortly describe the key input parameters for our calculations.

Input for performing *VASP* calculations contains the following main files [49]:

I. POSCAR. This file describes atom positions and allows fixing of atomic coordinates if necessary (it can be used, for example, to calculate interstitial positions when geometry relaxation leads to the system of stable basic configuration). In all slab calculations, we perform partial or complete structure optimization within the supercell of fixed linear dimensions using criterion of the total energy minimization. Atom positions for each calculated system are defined in POSCAR file, according to crystallographic properties of studied structure.

II. POTCAR. This file contains information about such properties of different atoms as the RECP pseudopotentials, atomic masses, the energy of reference atomic configuration, which the pseudopotential was created for (more detailed information about pseudopotentials is contained in Subsection 3.3), *etc*.

Computational parameters must be defined in following two files:

III. KPOINTS. This file determines the *k*-point mesh in the BZ. In this study, we have generated *k*-points using the Monkhorst-Pack's technique [59] whereas the electron populations were determined following the method of Methfessel and Paxton [60] as implemented in the *VASP* code.

For each series of calculations, we have found the optimal *k*-point mesh that would provide the convergence of results: the $8 \times 8 \times 8$ mesh for bulk calculations, the $8 \times 8 \times 1$ mesh for major part of surface calculations (perfect UN surface, vacancies on the UN(001) surface, oxygen adsorption and migration, as well as oxygen incorporation into pre-existing N vacancies), as well as the $4 \times 4 \times 1$ mesh for calculations of

molecular oxygen interaction with UN(001) surface and for all UN(110) surface calculations (including molecular adsorption, vacancies on UN(110) surface, and oxygen incorporation).

IV. INCAR. This main *VASP* input file determines "what to do and how to do it". Complete list of keywords is enumerated in the *VASP* manual [49]. In following paragraphs we describe only those parameters which variation has been especially important for our calculations.

IVa. ISPIN. This option defines the spin-polarized calculations. For UN, as a system with magnetic properties, the key "yes" has been used always.

IVb. MAGMOM. This option defines the initial magnetic moment on each atom (the calculation begins from the defined magnetic moments, however, they are changed during this calculation). We have chosen initial ferromagnetic state for all UN calculations. If one is searching for a ferromagnetic solution, it is usually safest to start from the larger local magnetic moments. This is why for spin-relaxed FM calculations, we have started from the value of 2 μ_B *per* U atom. For spin-frozen FM calculations, we have started from the magnetic moment 1 μ_B *per* U atom.

IVc. NUPDOWN. This key fixes the spin moment of the whole system to specified value. For spin-frozen calculations, we suggest the magnetic moment 1 μ_B *per* U atom.

IVd. ENCUT. Selection of plane waves is determined by the cut-off energy E_{cut}. The optimal cut-off energy has been found to be equal to 520 eV.

IVe. ISMEAR. Determines how the partial occupancies are defined for each wavefunction.We use Gaussian smearing for our calculations.

IVf. SIGMA. This key, describing the difference between the free energy and the total energy, must be chosen as large as possible. The smearing parameter of 0.2 eV has been found to be optimal for reasonable convergence suggesting the electronic entropy contribution of the order of 10 meV.

IVg. NELMDL. This key gives the number of *non*-self-consistent steps at the beginning: if one initializes the wave functions randomly, the initial wave functions are far from anything reasonable. Choice of key "delay" for starting the charge density update becomes essential in all cases where the convergence is very poor [49]. In UN calculations, this value has been increased 3-5 times as compared to the default value (15-25 steps *vs.* 5 default steps).

IVh. ALGO. Different algorithms are implemented into *VASP* code. For example, fast but rough RMM-DIIS algorithm [49, 61] *vs.* slow but accurate Davidson blocked algorithm [49, 62]. Our experience shows that only application of the Davidson algorithm leads to reliable results. Unfortunately, computer recourses are always limited and calculations for some systems are very time-consuming. To resolve this problem for especially hard calculations, we have splitted calculations within two stages. At first stage, we have used RMM-DIIS to obtain roughly-relaxed geometry and approximate electronic density. At second stage, we have started from geometry and electronic density relaxed at first stage, using Davidson algorithm to obtain final results. This approach significantly decreases computational expenses for many complicated systems.

3.6. Computational parameters in LCAO *CRYSTAL-06* code

For LCAO calculations, the *CRYSTAL-06* code have been used [63], which applies the Gaussian-type functions centered on the atomic nuclei as the basis sets for expansion of the linear combination of atomic orbitals (LCAO) combined with the non-local exchange-correlation functional PBE [64]. The oxygen basis set (BS) 8-411G(1*d*) has been taken from Ref. [65]. For the N atom, the all-electron BS 6-311G(2*d*) has been used [66]. Finally, for the U atom, the three energy-adjusted relativistic core effective potentials have been used (the pseudopotential of Stuttgart-Cologne group, SC60, with 60 electrons in the core [67] as well as the two Mosyagin-Titov large-core (MT78) and small-core (MT60) pseudopotentials with 60 and 78 electrons in the core, respectively [68]) To avoid linear dependence of basis set in the *CRYSTAL* LCAO calculations, the diffuse *s*-, *p*-, *d*- and *f*- Gaussian-type orbitals with exponents < 0.2 a.u.$^{-1}$ have been removed from the basis sets. The exponents of other polarization functions have been reoptimized, to restore the required precision in the total energy. Prior to a study of surface properties, the bulk structure optimization of UN crystal has been performed using the LCAO approach. The Monkhorst-Pack scheme with 16 × 16 × 16 *k*-point mesh for the BZ sampling [59] and 32 × 32 × 32 *k*-point Gilat net for the calculation of the Fermi energy and density matrix [69] have been used for this purpose.

3.7. Slab model and defect periodicity

When performing PAW surface calculations, we simulate the UN surface using the symmetrical slabs containing odd number of atomic layers and separated by the vacuum gap of 38.9 Å which corresponds to 16 inter-layers for UN(001) surface (Fig. 3.1). These vacuum gaps are large enough, to exclude the direct interaction between the neighboring 2D slabs within 3D slab model. LCAO calculations do not require artificial repetition of 2D slab along the normal to the surface direction as it is realized in PW calculations.

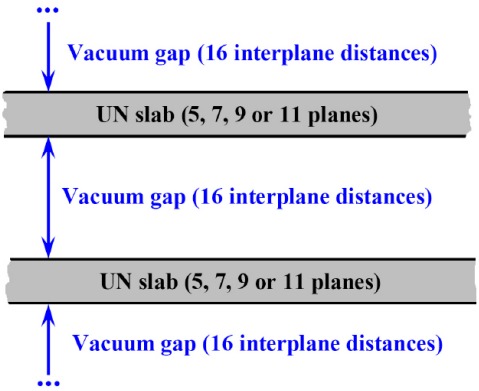

Figure 3.1. Cross-section of 3D model for UN slab.

To simulate single point defects (either N or U vacancies) and oxygen atom adsorbed on surface or incorporated into pre-existing vacancy as well as to reduce lateral interactions between them, we have applied a supercell approach, using 2 × 2 and 3 × 3 extensions of primitive unit cell (Fig. 3.2). These supercells contain four (2 × 2 supercell) and nine (3 × 3 supercell) pairs of N and U atoms in each defectless layer while periodically distributed surface vacancies (or oxygen atoms/molecules) *per* surface cell correspond to defect (oxygen) concentrations of 0.25 and 0.11 monolayers (ML), respectively. To reduce computational efforts, we have often considered the two-sided arrangement of the point defects which is symmetrical with respect to the central (mirror) plane. The suitable choice of supercell size is especially significant question. From one side, larger supersell is much closer to the model of isolated defect, on the other hand, this supercell requires considerably larger computational resourses (for example, 3 × 3 UN 7-layer supercell contains 126 atoms, *i.e.*, 2.25 times larger as compared to 56 atoms in 2 × 2 UN 7-layer supercell). In present study, we perform analysis of the finite-size effects in supercells of different sizes, to estimate deviation from the model of isolated defect.

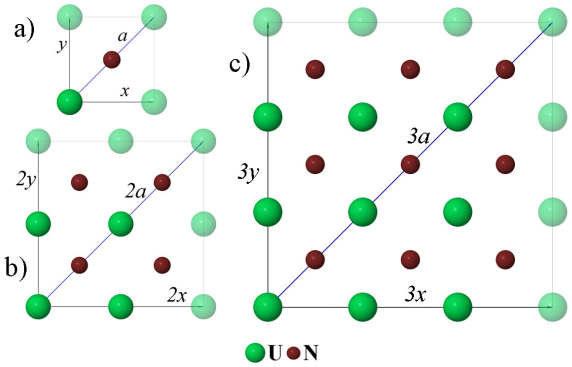

Figure 3.2. Atop views of primitive cell (a) as well as 2 × 2 (b) and 3 × 3 (c) supercells upon UN(001) surface. Here *x* and *y* axes coincide with directions of surface translation vectors while *a* is lattice constant. Half-shaded atoms show borders of chosen surface cells.

4. Modeling of UN bulk

The global aim of this stydy is to understand the mechanism of oxygen adsorption as well as further oxidation of uranium nitride. The first step of the current theoretical study is to develop methodology for correct description of ideal bulk and surface properties as performed in Refs. [P1, P4]. At a second step, this methodology can be applied to study defective surfaces as well as adsorption of oxygen atoms and molecules on perfect or defective surface. The results of DFT-PW calculations on UN bulk, perfrect surface and atomic oxygen adsorption upon it were compared with the corresponding DFT-LCAO results obtained by group of Prof. R.A. Evarestov (*St. Petersburg State University*).

Before calculations on UN surface, we must consider UN bulk and estimate its bulk properties. The main results obtained in bulk calculations are collected in Table 4.1, which shows that the cohesion energy E_c is essentially underestimated in LCAO MT78 calculations and slightly underestimated in PW calculations. The value of E_c is close to the experimental value in while in LCAO MT60 and SC60 calculations. As to the lattice parameter *a*, its DFT-LCAO values are underestimated (4.78 Å and 4.80 Å) but they do not differ too much from those obtained in DFT-PW calculations performed by us and other authors, being very close to experimental value. The optimized lattice constant (4.87 Å for PAW *VASP vs.* 4.81 Å for LCAO *CRYSTAL* calculations) has been used in all our further calculations.

Table 4.1. The results of calculations on UN bulk: the cohesive energy E_c (eV), the lattice constant a_0 (Å) and the bulk modulus B (GPa). The experimental values are given in brackets in the first column. The spin density (SD) for U atom is given in μ_B.

Property (experimental [1])	PW (*VASP*)		PW (other theoretical studies)		LCAO (Prof. R. Evarestov group)		
	PW91	PBE	PW91 PAW [33]	PBE AE-LAPW [20, 25]	MT78	MT60	SC60
a_0, Å (4.886)	4.868	4.867	4.864	4.886	5.17	4.78	4.80
E_c, eV (13.6)	14.79	14.57	14.7	13.4	9.6	13.4	13.6
B (194)	227	224	226	209	167.2	291.6	276.9
Q_U, *e*	1.69	1.69	1.61	-	1.63	1.55	1.58
SD, μ_B	1.15	1.19	1.05	1.25	3.18	1.18	1.06

The bulk modulus *B* is overestimated in both PW and LCAO (MT60 and SC60) calculations and underestimated in MT78 calculations. The calculated effective charge of U atom (Q_U) in UN is close to 1.6 *e* for all three LCAO RECP pseudopotentials used and comparable to 1.7 *e* for PW calculations using the topological Bader analysis. A comparison of LCAO (RECP 60) and the PW (RECP 78) results demonstrates a qualitative correlation of properties calculated using both methods, except for bulk modulus which is noticeably overestimated in the *CRYSTAL* calculations as compared to the experimental value.

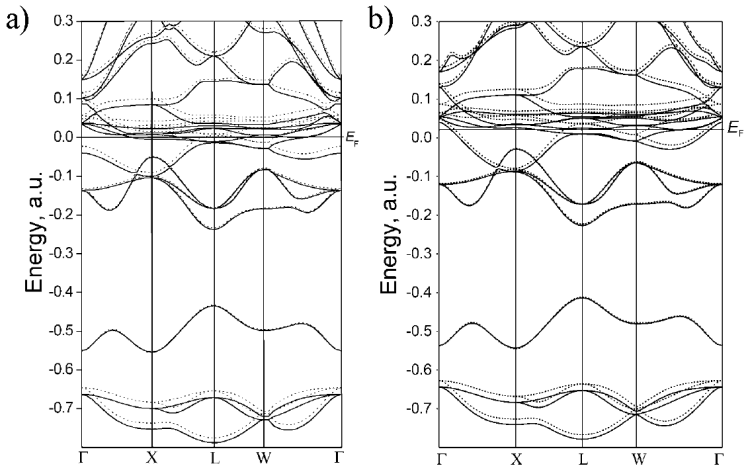

Figure 4.1. The energy bands of UN crystal constructed using: a) PW PW91 (RECP SC78) and b) LCAO PW91 (RECP SC60) Hamiltonians. The energies are given in a.u., solid and dotted lines correspond to the states with spin up and spin down, respectively.

The band structures for UN bulk calculated using the two above-mentioned methods (DFT and LCAO), when applying the same PW91 Hamiltonian, are presented in Fig. 4.1. Band structures demonstrate good correlation between both approaches, even at quantitative level, especially below the Fermi level, being in agreement with the experiment [12] and the DOS analysis performed in previous PW *VASP* calculations [34].

The results of DFT-PW calculations on the lattice constant, bulk modulus, cohesive energy, charge distribution and band structure for UN single crystal are obtained. The results of DFT-PW calculations on UN bulk were compared with the corresponding DFT-LCAO results obtained by group of Prof. R.A. Evarestov. The results of PW and LCAO calculations on UN bulk demonstrate a good qualitative agreement between them.

5. Structural properties of UN (001) and (110) surfaces

Synthesized specimens of polycrystalline UN contains particles with differently oriented crystallographic facets [9]. To simplify modeling of the oxygen interaction with UN surface, we study in this PhD work mainly the (001) surface since according to Tasker analysis [70] it has the lowest surface energy. Nevertheless, real UN particles (Fig. 2.2) contain facets with different crystallographic orientation. To increase validity of our results, we have additionally performed (110) surface calculations. We chose (110) surface orientation for additional calculations since alternative low-indiced (111) surface contains charged planes and its calculation requires artificial approaches. Moreover, strong reconstruction must occur, in order to stabilize polar (111) surface, similarly to MgO(111) [71]. Less densely-packed UN(110) surface is characterized by smaller interlayer distance in *z* direction as compared to (001) surface (Table 5.1 and Fig. 5.1).

Table 5.1. Comparison between the UN(001) and UN(110) surfaces (*a* is a lattice constant of cubic *fcc* crystal).

	(001) surface	**(110) surface**
Size of surface unit cell (Å x Å)	3.44 × 3.44 $(\frac{\sqrt{2}}{2}a \times \frac{\sqrt{2}}{2}a)$ or $(\frac{1}{2}a \times a)$	4.87 × 3.44 $(a \times \frac{\sqrt{2}}{2}a)$
Distance between two nearest U and U (or N and N) atoms in *xy* plane (Å)	3.44 $(\frac{\sqrt{2}}{2}a)$ in both directions	4.87 in *x* direction 3.44 in *y* direction
Distance between nearest U and N atoms in *xy* plane (Å)	2.435 $(\frac{a}{2})$	2.435 $(\frac{a}{2})$ in *x* direction not defined in *y* direction
Distance between neighbor layers in z direction (Å)	2.435 $(\frac{a}{2})$	1.72 $(a\frac{\sqrt{2}}{4})$
Distance between nearest atoms in *z* direction (Å)	2.435 $(\frac{a}{2})$, distance between U and N atoms	3.44 $(\frac{\sqrt{2}}{2}a)$, distance between N and N (or U and U) atoms

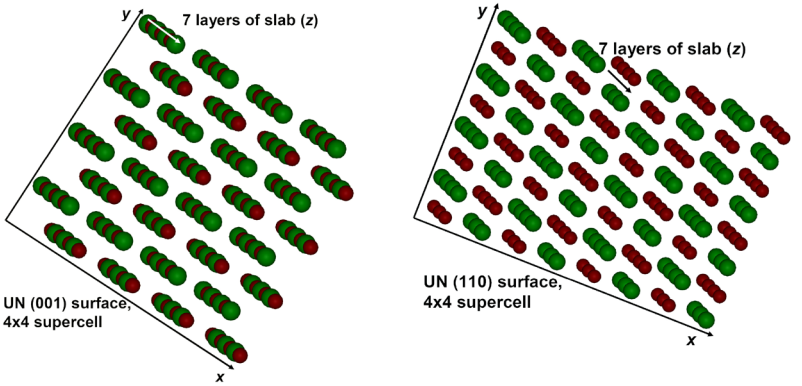

Figure 5.1. Structural comparison of slabs used for simulation of (001) (a) and (110) (b) UN surfaces.

We simulated reconstruction of perfect and defective UN(110) surface as well as atomic oxygen adsorption, formation of N vacancies and oxygen incorporation into them. These results are distributed in the corresponding subsections of Sections 6-8.

6. Modeling of perfect UN surface

As has been mentioned in Section 2.1, experiment shows that UN bulk undergoes the AFM ordering below 53 K [5]. We have performed the calculations on both FM and AFM states. Our PAW test calculations on UN bulk have shown that the FM phase is energetically slightly more favorable than AFM phase. Analogous results were obtained using LCAO method as applied by group of Prof. R.A. Evarestov. Due to a small diference between the energies in FM and AFM states (~0.001-0.01 eV) and due to a complicated magnetic structure of UN surface [31], only FM state has been considered in our UN surface calculations.

6.1. Spin-frozen PW and LCAO calculations on defectless UN(001) surface

Analogously to perfect bulk calculations, we compare results of PW and LCAO calculations on UN(001) surface. Aperiodic (2D) and periodic (3D) models in regards to the direction normal to the slab have been used for LCAO and PW calculations, respectively [51].

We have analyzed in detail the vertical displacements (along *z* axis) of both surface and subsurface atoms from their host lattice sites in UN bulk (Table 6.1), effective atomic charges (Table 6.2), the surface energies (Table 6.3) as well as DOS obtained in the PW calculations (Fig. 6.2).

Surface energy of an *n*-layer slab has been estimated from the standard basic relationship:

$$E_{surf}(n) = \frac{1}{2S}(E_n - nE_b) \qquad \textit{(Eq. 6.1.1)}$$

where E_n is the total slab energy *per* primitive surface unit cell and *S* its area, while E_b the total energy *per* primitive bulk unit cell (Fig. 6.1).

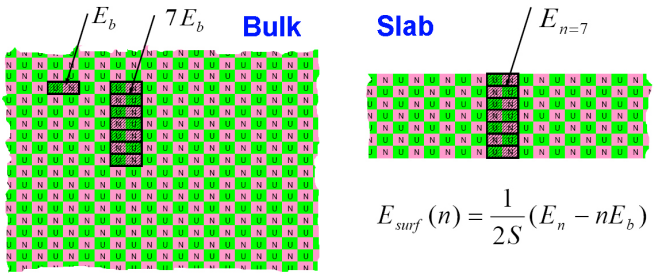

Figure 6.1. Surface energy calculated for 7-layer slab. E_n is the total slab energy *per* primitive surface unit cell, E_b is the total energy *per* primitive bulk unit cell, n is number of layers, S is unit cell surface area.

There is a good qualitative agreement between structural relaxations and effective atomic charges for the LCAO and PW data. First of all, in both methods atomic displacements have the same directions: N atoms go outside the surface whereas U atoms relax towards the slab center. This is a pattern typical for the rumpling observed on oxide surfaces. There have been also observed substantially larger magnitudes of surface U displacements as compared to N atoms, whereas subsurface atom relaxations are smaller.

Table 6.1. The calculated atomic displacements Δz (Å) on UN(001) obtained for different slabs and methods. Positive sign means an outward displacement from the slab center.

Atom	Method	Number of atomic layers in slab				
		3	5	7	9	11
surface U	LCAO	-0.085	-0.095	-	-	-
	LCAO (extra layer added)	-0.026	-0.046	-	-	-
	PW PW91	-0.041	-0.046	-0.050	-0.061	-0.057
subsurface U	LCAO		-0.011	-	-	-
	LCAO (extra layer added)		-0.013	-	-	-
	PW PW91		-0.018	-0.016	-0.013	-0.013
surface N	LCAO	0.064	0.058	-	-	-
	LCAO (extra layer added)	0.049	0.025	-	-	-
	PW PW91	0.030	0.022	0.025	0.033	0.026
subsurface N	LCAO		-0.002	-	-	-
	LCAO (extra layer added)		0.014	-	-	-
	PW PW91		0.026	0.028	0.032	0.022

Table 6.2. The effective atomic charges $q(e)$ on UN(001) slab

Atom	Method	Number of atomic layers in slab				
		3	5	7	9	11
surface U	LCAO	1.63	1.63	-	-	-
	LCAO (extra layer added)	1.64	1.64	-	-	-
	PW PW91	1.65	1.66	1.72	1.67	1.65
subsurface U	LCAO	-	1.51	-	-	-
	LCAO (extra layer added)	-	1.55	-	-	-
	PW PW91	-	1.65	1.63	1.63	1.69
middle U (mirror plane of slab)	LCAO	1.45	1.57	-	-	-
	LCAO (extra layer added)	1.52	1.55	-	-	-
	PW PW91	1.62	1.67	1.72	1.65	1.62
surface N	LCAO	-1.55	-1.55	-	-	-
	LCAO (extra layer added)	-1.61	-1.60	-	-	-
	PW PW91	-1.64	-1.63	-1.64	-1.63	-1.67
subsurface N	LCAO	-	-1.59	-	-	-
	LCAO (extra layer added)	-	-1.57	-	-	-
	PW PW91	-	-1.67	-1.7	-1.64	-1.7
middle N (mirror plane of slab)	LCAO	-1.61	-1.58	-	-	-
	LCAO (extra layer added)	-1.58	-1.57	-	-	-
	PW PW91	-1.65	-1.7	-1.66	-1.62	-1.64

The surface energies are partly stabilized for slabs containing at least 5-7 layers whereas the relaxation energy is more sensitive to the thickness (Table 6.3). Due to scarceness of experimental results, the calculated values of surface energy could be qualitatively compared only with 1.2 J/m^2 obtained recently for UO_2(001) surface energy using the first-priciples calculations [46]. As one can see, the surface energies of these surfaces are predicted to be similar. A qualitative agreement is observed between the UN(001) surface energies obtained using both LCAO and PW calculations.

Table 6.3. Surface energies E_{surf} (J · m^{-2}) and relaxation energies E_{rel} (eV) obtained for UN(001) surface in LCAO and PW calculations

Number of atomic layers in slab			3	5	7	9	11
Method	LCAO	E_{surf} (unrelaxed)	2.20	2.29	2.28	2.11	-
		E_{surf} (relaxed)	2.06	2.13	-	-	-
		E_{rel}	0.203	0.230	-	-	-
	LCAO (extra layer added)	E_{surf} (unrelaxed)	1.68	1.45	-	-	-
		E_{surf} (relaxed)	1.430	1.38	-	-	-
		E_{rel}	0.359	0.121	-	-	-
	Plane waves PW91	E_{surf} (unrelaxed)	1.81	1.87	1.84	1.86	1.90
		E_{surf} (relaxed)	1.70	1.69	1.70	1.70	1.69
		E_{rel}	0.156	0.258	0.210	0.239	0.305

The total and projected DOSs in the FM state obtained in our PAW calculations are present in Fig. 6.2. There is a small difference in band shapes as compared to previous UN bulk calculations [34], due to noticeably higher *k*-point mesh and cut-off energy used in our studies. A comparison of the bulk DOS (Fig. 6.2a) with that for the projections of the surface U and N atoms (Fig. 6.2b) shows mainly changes in the shape of unoccupied states above the Fermi level. In both cases, the mixed metallic-covalent bonding is observed for U(*5f*) states at the Fermi level which confirms results of previous experimental and theoretical studies.

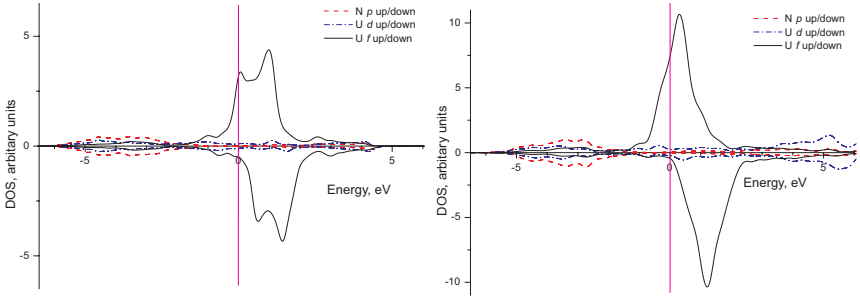

Figure 6.2. The projected DOS for UN bulk (a) and for perfect 7-layer UN(001) slab (b) in FM states.

6.2. Spin-relaxed PW calculations of defectless UN (001) and (110) surfaces

The results obtained in spin-relaxed PAW calculations on perfect UN (001) and (110) surfaces (Fig. 6.3) are discussed. The calculations of the effective atomic charges q^{eff}, atomic displacements Δr, average magnetic moments μ_{av} of U atoms, and surface energies E_{surf} for defect-free slabs of different thicknesses (Tables 6.4 and 6.5) have been performed, in order to check how these properties depend on atomic spin relaxation [P4]. The spin relaxation leads to considerable change of the E_{surf} depending on the number of layers in a slab (Table 6.4). The largest μ_{av} value was obtained for U atoms in the 5-layer slab, *i.e.*, μ_{av} slightly decreases with the thickness suggesting difference of 0.3 μ_B between the 5- and 11-layer slabs. The lattice relaxation energies in spin-relaxed calculations turn out to be quite small, *i.e.*, ~0.03 eV.

Depending on slab thickness, the surface energies are ~0.5-0.7 J·m^{-2} larger for UN(110) surface (Table 6.4). It means that the UN(001) surface is energetically more favorable.

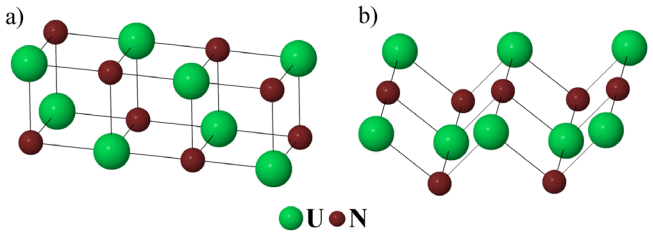

Figure 6.3. 2-layer models of UN(001) (a) and UN(110) (b) surfaces.

Table 6.4. Surface energies E_{surf} (J·m^{-2}) as well as averaged magnetic moment (in μ_B) of U atom for the defectless UN(001) and UN(110) surfaces. In spin-frozen calculations, μ was chosen to be 1 μ_B

Number of atomic layers	E_{surf} (J·m^{-2}) spin-frozen slab (001)	E_{surf} (J·m^{-2}) spin-relaxed slab (001)	$\mu_{av}(\mu_B)$ (001)	E_{surf} (J·m^{-2}) spin-relaxed slab (110)	$\mu_{av}(\mu_B)$ (110)
5	1.69	1.44	1.57	1.977	1.645
7	1.70	1.37	1.44	1.928	1.464
9	1.70	1.29	1.37	1.878	1.417
11	1.69	1.22	1.33	1.830	1.385

It is also interesting to analyze q^{eff} values for atoms across the slab as a function of the number of layers in a slab (Table 6.5). First, these q^{eff} show considerable covalent bonding both on the surface (*e.g.*, sub-surface) and on the central plane since the values. Second, due to different reconstruction mechanisms of UN(001) and UN(110) surfaces, the atomic charges are different too: ionicity of bonds at (001) surface is higher, thus leading to certain difference in surface properties. Third, the atomic charges depend on

both the spin relaxation and the number of layers (*cf.* results of spin-relaxed calculations and spin-frozen PW calculations presented in Tables 6.5 and 6.2, respectively).

Table 6.5. Atomic Bader charges for the defectless spin-relaxed UN (001) and (110) surfaces.

	Number of UN(001) slab atomic layers				Number of UN(110) slab atomic layers			
Atom	**5**	**7**	**9**	**11**	**5**	**7**	**9**	**11**
Surface U	1.68	1.74	1.68	1.72	1.46	1.48	1.49	1.48
Sub-surface U	1.67	1.63	1.63	1.67	1.88	1.85	1.83	1.84
U in central (mirror) plane	1.69	1.72	1.65	1.66	1.60	1.74	1.64	1.70
Surface N	-1.65	-1.67	-1.67	-1.68	-1.55	-1.55	-1.55	-1.55
Sub-surface N	-1.68	-1.70	-1.70	-1.67	-1.75	-1.73	-1.75	-1.73
N in central (mirror) plane	-1.74	-1.65	-1.65	- 1.63	- 1.70	-1.71	-1.75	-1.74

Table 6.6. Atomic displacements Δz(Å)* for defectless UN (001) and (110) surfaces.

Number of atomic layers	U atom displacements				N atom displacements			
	(001) surface		(110) surface		(001) surface		(110) surface	
	Surface	**Sub-surface**	**Surface**	**Sub-surface**	**Surface**	**Sub-surface**	**Surface**	**Sub-surface**
5	-0.050	-0.012	-0.053	-0.005	0.023	0.023	-0.279	0.068
7	-0.046	-0.009	-0.038	-0.009	0.024	0.028	-0.272	0.092
9	-0.047	-0.011	-0.042	-0.014	0.024	0.028	-0.279	0.091
11	-0.047	-0.011	-0.015	0.015	0.025	0.031	-0.252	0.118

* negative sign means an inward atomic displacement towards the mirror plane of slab

The atomic displacements Δz from perfect lattice sites differ significantly for U atoms positioned at the surface and sub-surface layers (Table 6.6) being somewhat larger for the 5-layer slab while displacements of nitrogen atoms for all the slabs remain almost unchanged. Note that N atoms on (001) surface are displaced up whereas U atoms are shifted inwards the slab center which results in the surface rumpling up to 1.2% of the lattice constant. In contrary, the surface U atoms of rumpled UN(110) surface lie higher than the corresponding N atoms which well illustrates the difference of charges and other surface properties mentioned above.

6.3. Perfect UN surface calculations: summary

Our defectless surface modeling shows metallic properties of UN surface, analogously to previous bulk calculations. We compared results for DFT PW and LCAO calculations and found a good corellation between both approaches. Comparison of UN(001) and UN(110) surfaces shows that the former is energetically more favorable. The surface energies depending of slab thickness are equal to 1.22-1.44 $J \cdot m^{-2}$ for UN(001) *vs.* 1.83-1.98 $J \cdot m^{-2}$ for UN(110) surface. This fact allow us to perform both calculations on defectless UN surface and oxygen adsorbtion upon the (001) surface mainly.

7. Modeling of single N and U vacancies

7.1. Vacancy calculations: model and formation energies

To understand the oxidation mechanism in more detail, one has to take into account *surface defects* and their interaction with oxygen. For this reason, we studied basic properties of *surface* vacancies [P4]. We have calculated not only the outermost surface defects, but also the sub-surface defects as well as those positioned at the central layer of the slab. We have considered the two-sided arrangement of the point defects which is symmetrical with respect to the central (mirror) plane (the atomistic model of surface N vacancies with the 2×2 periodicity of defects is shown in Fig. 7.1). The FM state has been chosen for all our slab calculations performed for the self-consistent (relaxed) atomic magnetic moments with no spin-orbit interactions included. We have performed the total spin relaxation in the system.

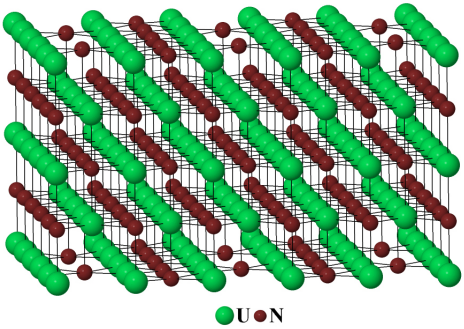

Figure 7.1. 5-layer UN(001) slab containing the two-sided surface N vacancies distributed with a 2×2 periodicity.

The formation energy of point defect is calculated either as

$$E_{form}^{\mathrm{N(U)}vac} = \frac{1}{2}\left(E^{\mathrm{UN(U/N\_vac)}} + 2E_{ref\_\mathrm{I(II)}}^{\mathrm{N(U)}} - E^{\mathrm{UN}}\right), \qquad \textit{(Eq. 7.1.1a)}$$

for surface and sub-surface vacancies, or

$$E_{form}^{\mathrm{N(U)}vac} = E^{\mathrm{UN(U/N\_vac)}} + E_{ref\_\mathrm{I(II)}}^{\mathrm{N(U)}} - E^{\mathrm{UN}}, \qquad \textit{(Eq. 7.1.1b)}$$

for a vacancy in the central layer of the slab. Here $E^{\mathrm{UN(U/N\_vac)}}$ is the total energy of fully relaxed slab containing N (or U) vacancies, E^{UN} the same for a defect-free slab, while $E_{ref\_\mathrm{I(II)}}^{\mathrm{N(U)}}$ is reference energy for N (or U) atom. In the present study, we have considered the two reference states for calculations of the defect formation energy, both are widely used in the literature.

The first reference corresponds to N (U) isolated atom in triplet (quartet) spin states determined by $2p^3$ ($5f^36d^1$) valence electron configurations (hereafter, reference I as in Table 7.1) calculated in a large rectangular parallelepiped box ($28.28 \times 28.28 \times 22$ Å^3), *i.e.*:

$$E^{\mathrm{N(U)}}_{ref\_\mathrm{I}} = E^{\mathrm{N(U)}}_{atom}. \qquad \textit{(Eq.7.1.2)}$$

The second reference state (hereafter, reference II as in Table 7.1) represents the chemical potential of N (U) atom which is defined as a function of temperature and partial nitrogen pressure. By neglecting these effects, the N chemical potential can be treated as the energy of atom in the molecule N_2. Consequently, the chemical potential of U atom is given by the one-half total energy (*per* unit cell) of U single crystal in its low-temperature α-phase having the orthorhombic structure [72]. Thus, the corresponding second reference energies can be estimated as:

$$E^{\mathrm{N}}_{ref\_\mathrm{II}} = \mu_{\mathrm{N}_2} = \frac{1}{2} E_{tot}\left[\mathrm{N}_2\right], \qquad \textit{(Eq.7.1.3a)}$$

$$E^{\mathrm{U}}_{ref\_\mathrm{II}} = \mu_{\alpha\text{-U}} = \frac{1}{2} E_{tot}\left[\alpha\text{-U}\right], \qquad \textit{(Eq.7.1.3b)}$$

where $E_{tot}[N_2]$ is the total energy of nitrogen molecule while E_{tot}[α-U] the total energy of U bulk unit cell containing two atoms. The chemical potentials of N and U, as calculated according to *Eq. 7.1.3*, represent extreme cases of N(U)-rich conditions [73], *i.e.*, their minimum values have not been considered in the present study. The formation energy of N (U) vacancy with respect to the N_2 molecule (or α-U single crystal) and the energy of N (U) isolated atom are closely related: the former being larger than the latter by half the binding energy of the N_2 molecule or half the cohesive energy of α-U single crystal.

The optimized lattice parameters of α-U (a = 2.80 Å, b = 5.88 Å, c = 4.91 Å) have been slightly underestimated as compared to values obtained experimentally [72] and calculated elsewhere [74, 75], except for the parameter b which is in a good agreement with experimental value of 5.87 Å [72] (while a = 2.86 Å, c = 4.96 Å [72]). Also, the ratios c/a, b/a as well as the parameter c are well verified by another plane-wave DFT study [41]. Analogously to an isolated nitrogen atom, the N_2 molecule has been calculated in the cubic box but of a smaller size ($8 \times 8 \times 8$ Å^3). The molecule N_2 is characterized by the bond length of 1.12 Å and the binding energy of 10.63 eV being well comparable with the experimental values of 1.10 Å and 9.80 eV [76], respectively. The pre-factor of ½ in *Eq. 7.1.1a* arises due to a mirror arrangement of two N(U) vacancies on the surface and sub-surface layers (Fig. 7.1).

The formation energies of N and U vacancies ($E^{\mathrm{N(U)}\,vac}_{form}$) calculated using *Eqs. 7.1.1-7.1.3* (with the two reference states) as functions of the slab thickness are collected in Table 7.1. These are smallest for the surface layer and considerably increase (by ~0.6 eV for the N vacancy and by ~1.7 eV for the U vacancy) in the sub-surface and central layers, independently of the reference state. This indicates the trend for vacancy segregation at the interfaces (surface or crystalline grain boundaries). A weak dependence of $E^{\mathrm{N(U)}\,vac}_{form}$ on the slab thickness is also observed. The value of $E^{\mathrm{N(U)}\,vac}_{form}$ is saturated with the slab thicknesses of seven atomic layers and more. Moreover, the difference between values of $E^{\mathrm{N(U)}\,vac}_{form}$ for the 5- and 7-layer slabs is less for the surface vacancies than for those in the central layer. This difference is the largest for the U vacancy in the central plane (~0.16 eV).

The reference state II leads to smaller $E_{form}^{N(U)\,vac}$ (as compared to those found for the reference state I) and demonstrates a significant difference for two types of vacancies. According to reference II, the U vacancy could be substantially easier formed at T = 0 K than the N vacancy. Notice that the chemical potentials of O and U atoms used in similar defect studies on UO_2 bulk did not reveal the energetic preference for U vacancy [75, 77]. The defect-defect interaction is not responsible for this effect as $E_{form}^{N(U)\,vac}$ decreased by 0.1 eV only with the larger supercell size (3 × 3 in Table 7.1). On the other hand, due to the temperature dependence of the chemical potential of a free N_2 molecule [78], we predict reduction of the formation energy of the N vacancy by ~0.8 eV as the temperature increases from room temperature up to 1000 °C. Unlike the reference state II, the reference I results in similar formation energies for both types of the vacancies. In the central slab layer, values of $E_{form}^{N(U)\,vac}$ are similar to those in the bulk (Table 7.1).

Table 7.1. The vacancy formation energies (in eV) for the two reference states (see the text for details).

Layer	Number of layers and supercell size	Reference I, Eqs. (7.1.1a)–(7.1.2)[a]		Reference II, Eqs. (7.1.1a), (7.1.1b), (7.1.3a) and (7.1.3b)[b]	
		U	N	U	N
Surface layer	5, 2 × 2	8.63	8.84	1.46	3.70
	7, 2 × 2	8.61	8.84	1.44	3.70
	9, 2 × 2	8.61	8.84	1.44	3.71
	11, 2 × 2	8.60	8.85	1.43	3.71
	5, 3 × 3	8.51	8.78	1.34	3.64
	7, 3 × 3	8.47	8.78	1.30	3.65
Sub-surface layer	5, 2 × 2	10.31	9.38	3.14	4.25
	7, 2 × 2	10.29	9.46	3.12	4.33
	9, 2 × 2	10.26	9.46	3.09	4.33
	11, 2 × 2	10.26	9.46	3.09	4.33
	7, 3 × 3	10.18	9.47	3.01	4.34
Central (mirror) layer[c]	5, 2 × 2	10.20	9.48	3.03	4.34
	7, 2 × 2	10.36	9.57	3.19	4.43
	9, 2 × 2	10.34	9.55	3.17	4.42
	11, 2 × 2	10.39	9.56	3.22	4.42
	7, 3 × 3	10.23	9.55	3.06	4.42

[a] reference energies I equal to -4.10 eV for U atom and -3.17 eV for N atom,
[b] reference energies II equal to -11.28 eV for U atom and -8.30 eV for N atom,
[c] defect formation energies for UN bulk using reference state I are 9.1-9.7 eV for N vacancy and 9.4-10.3 for U vacancy [34]

7.2. Surface reconstruction induced by vacancies

The local atomic displacements around the vacancies are largest for the nearest neighbors of vacancies. The analysis of atomic displacements allows us to suggest that the U vacancy disturbs the structure of the surface stronger than the N vacancy. If the N vacancy lies in the surface layer, displacements of the nearest U atoms in *z*-direction achieve 0.02-0.05 Å towards the central plane of slab. The displacements of N atom nearest

to surface N vacancy achieve 0.05 Å towards the central plane (*z*-direction) and 0.01 Å in the surface plane (*xy*-displacement). Maximum displacements of neighbor atoms around the N vacancy in the central plane have been found to be 0.04-0.07 Å (nearest U atoms from the neighboring layers are shifted in *z*-direction towards the vacancy) not exceeding 0.025 Å for all the other atoms in the slab.

In contrary, the U vacancy results in much larger displacements of neighboring atoms, irrespectively of its position. If this vacancy lies in the surface layer, the displacements of 0.3-0.32 Å for the nearest N atoms are observed. If the U vacancy lies in the central layer, the nearest N atoms from this layer are displaced by 0.17 Å while the N atoms from the nearest layers are not shifted in *xy*-direction, being shifted by 0.15 Å towards the slab surface in the *z*-direction. The atomic displacements around the vacancies in the UN bulk have been found to be –0.03 Å and 0.13 Å for N and U vacancies, respectively [34]. These values are close to those found in the present calculations for the vacancies in the central slab layer, which mimics the crystal bulk.

7.3. Electronic properties: Finite-size effects and choice of supercell size

The finite slab-size effects caused by relatively large concentration of defects could be illustrated using the difference electron density redistribution $\Delta\rho(\mathbf{r})$. In Fig. 7.2, these redistributions are shown for N vacancies positioned at both the outer (surface) and the central (mirror) planes of 5- and 7-layer slabs.

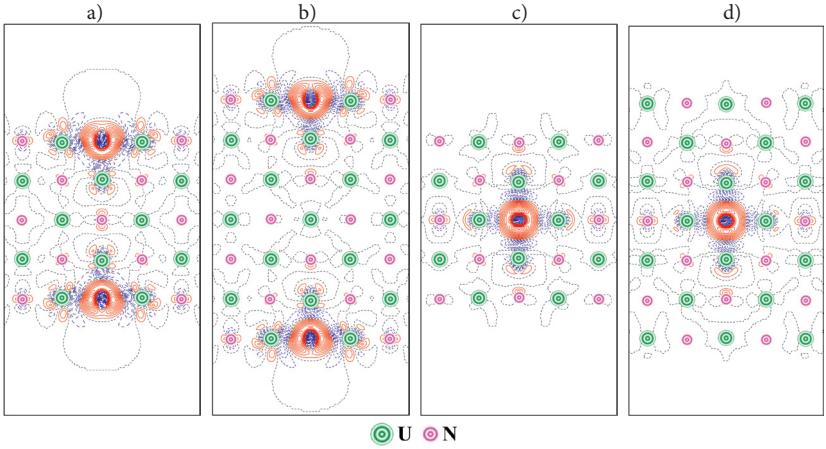

Figure 7.2. 2D sections of the electron density redistributions around the nitrogen vacancies in five- and seven-layer UN(001) slabs with 2 × 2 supercell extension defined as the total electron density of defected surface minus a superposition of the electron densities for both perfect surface and isolated atom in the regular position on the surface: a) N vacancy in a surface plane, five-layer slab, b) the same, 7-layer slab, c) N vacancy in a central plane, five-layer slab, d) the same, 7-layer slab. Solid (red) and dashed (blue) isolines correspond to positive (excess) and negative (deficiency) electron density, respectively. Isodensity increment is 0.25 e a.u.$^{-3}$.

Presence of two symmetrically positioned vacancies in the 5-layer slab induces their weak interaction across the slab (Fig. 7.2a) illustrated by appearance of an additional electron density around the N atoms in the central plane of the slab. Similarly, the vacancy in the mirror plane disturbs the atoms in the surface plane if thin slab contains only 5 layers (Fig. 7.2c). By increasing the slab thickness, we can avoid the effect of finite-slab size (Figs. 7.2b,d) which explains the stabilization of formation energies calculated for the 7-layer and thicker UN(001) slabs (Table 7.1).

The densities of states (DOS) are presented in Fig. 7.3. for both perfect and defective 7-layer UN slab. In accordance with previous bulk calculations, the U(5*f*) electrons are localized close to the Fermi level (Fig. 7.3a). These electrons are still strongly hybridized with the N(*2p*) electrons. It confirms the existence of covalent bonding observed in the analysis of Bader charges for defectless surface (Table 6.5). The N(2*p*) states form a band of the width ~4 eV, similar to that obtained in the bulk [P1, 34]. In contrast, the contribution of U(6*d*) electrons remains insensitive to the presence of vacancies since the corresponding levels are almost homogeneously distributed over a wide energy range including the conduction band. The visible difference of total DOS profiles in Fig. 7.3a and Fig. 6.2b for perfect 7-layer UN(001) slab can be explained by different slab geometry relaxation when performing spin-relaxed and spin-frozen calculations, respectively.

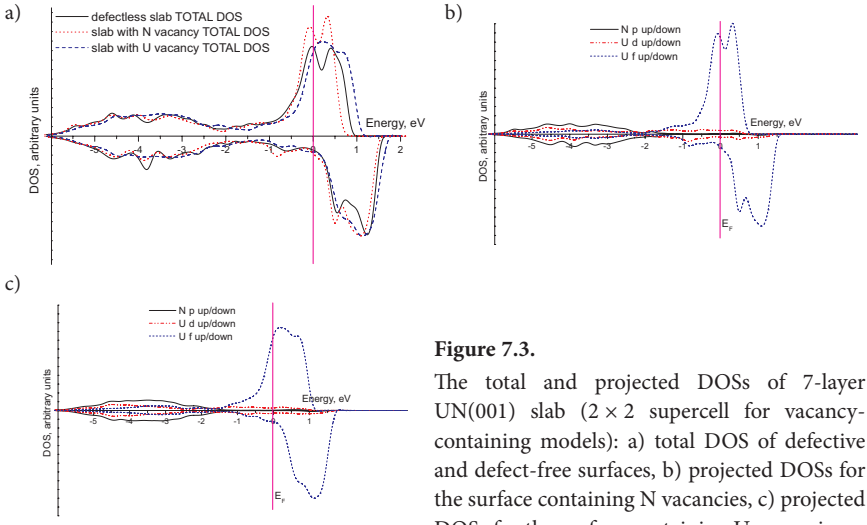

Figure 7.3.
The total and projected DOSs of 7-layer UN(001) slab (2 × 2 supercell for vacancy-containing models): a) total DOS of defective and defect-free surfaces, b) projected DOSs for the surface containing N vacancies, c) projected DOSs for the surface containing U vacancies.

7.4. Magnetic properties

The analysis of the averaged magnetic moment of U atoms (μ_{av}^{U}) in the defective UN slabs is done too (Fig. 7.4). It decreases for both types of vacancies as a function of a number of layers in the slab, except for the U vacancy in the surface layer which remains

almost unchanged. On the other hand, μ_{av}^{U} increases significantly when the U vacancy is located in the subsurface and surface layers. In contrast to the U vacancies, μ_{av}^{U} for the slabs with the N vacancies are less sensitive to the position of defect, they are practically identical for the slabs with the N vacancies in the surface and subsurface planes.

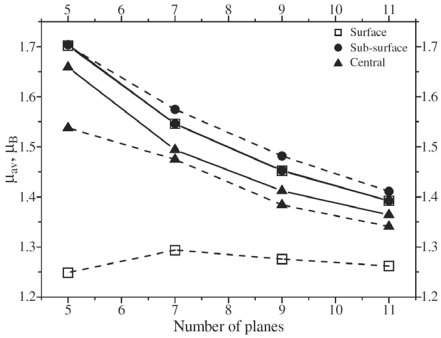

Figure 7.4. The averaged U magnetic moment μ_{av} (in μ_B) in the slab as a function of a number of planes. The dashed curves correspond to U vacancy whereas the solid curves describe the N vacancy.

7.5. Comparison of results for N vacancies on UN (001) and (110) surfaces

To increase the reliability of the results we also compare the results of calculations on N vacancies in surface layer upon UN(001) with analogous calculations on (110) surface (Fig. 7.5). For (110) surface, we have used 5-, 7-, 9- and 11-layer 2 × 2 surface supercells as well as 7-layer 3 × 3 supercell. Obtained results are presented in Table 7.2. All basic tendencies remain similar for vacancies on (110) surface. Averaged magnetic moment μ_{av} decreases as a function of a number of layers in the slab for both surfaces. On the other hand, vacancy formation energies are by ~0.7 eV smaller for UN(110) surface. This distinction is easy explainable due to a larger friability of the (110) surface as compared to the (001) surface.

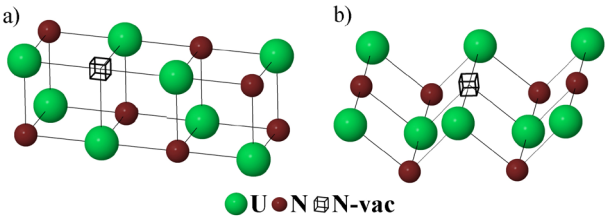

Figure 7.5. 2-layer models of N vacancy on UN (001) (a) and (110) (b) surface.

Table 7.2. Nitrogen vacancy formation energies (in eV) as well as averaged magnetic moment μ_{av} of U atom evaluated for UN (001) and (110) surfaces.

Number of layers and supercell size	N vacancy E_{form} on (001) surface	$\mu_{av}(\mu_B)$ (001)	N vacancy E_{form} on (110) surface	$\mu_{av}(\mu_B)$ (110)
5, 2 × 2	3.700	1.702	3.075	1.818
7, 2 × 2	3.706	1.548	3.028	1.585
9, 2 × 2	3.708	1.452	3.036	1.512
11, 2 × 2	3.712	1.392	3.026	1.453
7, 3 × 3	3.646	1.487	2.966	1.498

7.6. Vacancy calculations: summary

The formation energies for U and N vacancies have been determined using the two reference states, which include the energies of isolated atoms as well as atoms in the metallic α-U phase and N_2 molecule, respectively. The formation energies have indicated a clear trend for segregation towards the surface (and probably, grain boundaries) as these energies for surface layer are noticeably smaller than those for sub-surface and central layers (although both latter are very close). However, the magnetic moments in the subsurface and central layers differ significantly. We have demonstrated also a considerable deviation of effective atomic charges from formal charges (caused by a covalent contribution to the U-N bond).

8. Modeling of O adsorption and migration on perfect UN surface

8.1. Atomic oxygen adsorption

8.1.1. Model and theoretical background

To simulate the O atom adsorption, the 5-layer slabs with 2 × 2 supercell have been used for our PW calculations and spin-frozen LCAO calculations performed by group of Prof. R.A. Evarestov [P2]. The 5- and 7-layer 3D slabs with 2 × 2 and 3 × 3 supercells were used for our spin-relaxed PW calculations. To reduce computational efforts, we have considered symmetric two-sided arrangement of oxygen adatom (Fig. 8.1) similarly to calculations on vacancies.

Only ferromagnetic UN ground state has been considered in this study as the energetically most preferable state for low-temperature calculations. The calculations of UN bulk structure suggest the magnetic moment on the U atom ~1 μ_B. For *CRYSTAL* calculations and selected *VASP* calculations, we have fixed the total spin of the system. Thus, for five-layer slab the total magnetic moment of a 2 × 2 supercell (containing 20 U and 20 N atoms) in spin-frozen calculations was fixed at 20 μ_B.

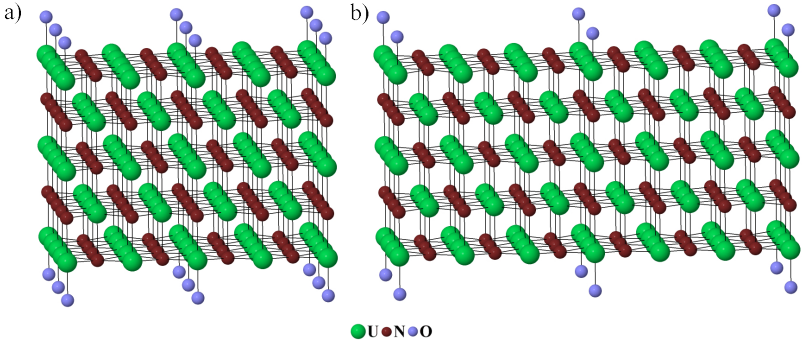

Figure 8.1. Model of O/UN(001) interface: two-sided adsorption of O atoms regularly distributed atop U_{surf} atoms with 2 × 2 (a) and 3 × 3 (b) periodicity.

The binding energy E_{bind} of adsorbed oxygen atom (O_{ads}) was calculated with respect to a free O atom:

$$E_{bind} = \frac{1}{2}\left(E^{UN} + 2E^{O_{triplet}} - E^{O/UN}\right), \qquad \textit{(Eq. 8.1.1)}$$

where $E^{O/UN}$ is the total energy of relaxed O/UN(001) slab for O_{ads} positions atop either the N or U surface ions, $E^{O_{triplet}}$ and E^{UN} the energies of an isolated O atom in the ground (triplet) state and of a relaxed UN slab. In PAW calculations, of free O atom, the

cubic box with edge ~20 Å has been used. The factor ½ before brackets appears since the substrate is modeled by slab with the two equivalent surfaces and O_{ads} is positioned symmetrically with respect to the surfaces.

8.1.2. *Comparison of spin-frozen PW and LCAO calculations on atomic adsorbtion*

The corresponding results of *VASP* and *CRYSTAL* calculations based on the two very different methods demonstrate a good qualitative agreement for O adatom properties atop the surface U atom (Fig. 8.2): the binding energies (3D slab models usually underestimate this parameter, due to a weak repulsion between the adjacent polarized slabs), atomic displacements and effective charges (which are calculated using the very different Mulliken (LCAO) and Bader (PAW) procedures).

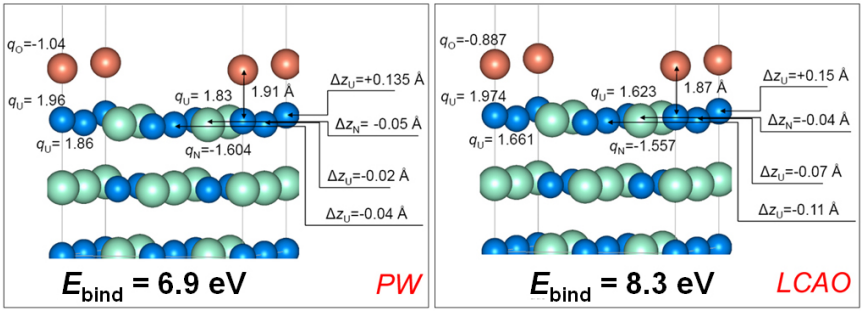

Figure 8.2. The calculated binding energy (E_{bind}), the distance between O and surface U cation ($d_{O\text{-}U}$), the effective atomic charges (q), and vertical (Δz) displacements of U and N atoms from the surface plane for adatom position atop the surface U atom calculated with PW and LCAO methods.

8.1.3. *PW calculations on binding energies, charges and structure relaxation*

Due to a mixed metallic-covalent nature of the chemical bonding in UN, we expect a high affinity of O_{ads} towards the UN(001) substrate. The binding energy *per* O adatom is expected to be closer to that on a regular O/Al(111) or O/Al(001) metallic interfaces (~10 eV) [79] than on semiconducting O/$SrTiO_3$(001) interfaces (with two possible SrO- or TiO_2-terminations) (~2 eV) [80]. Indeed, we have obtained in the *VASP* calculations the binding energies of 6.9-7.6 and 5.0-5.7 eV *per* O adatom atop the surface U or N ions, respectively, accompanied with 0.5-1.2 *e* charge transfer from the surface towards the O adatom (Tables 8.1 and 8.2). The positively charged surface U atom goes outwards, to the adsorbed O atom (Fig. 8.4), whereas in the O configuration atop the N atom, the latter is strongly displaced from the adsorbed O atom inwards the slab, due to a mutual repulsion between N and O.

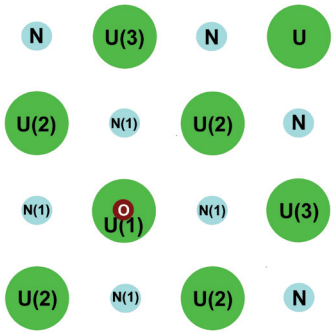

Figure 8.3.
Schematic view of O atoms adsorbed atop the surface U atom. Numbers enumerate non-equivalent surface atoms described in Tables 8.1 and 8.2.

Table 8.1. The calculated values of the binding energy (E_{bind}), the distance between O and surface U atom ($d_{O\text{-}U}$), the effective atomic charges on atoms (q), and vertical U and N displacements (Δz)[a] from the surface plane for adatom position atop the U_{surf}. Values of q for surface atoms on the perfect surface equal to +1.66 (+1.72) e for U_{surf} and −1.63 (−1.64) e for N_{surf} obtained in PAW 5-layer (7-layer) slab spin-frozen calculations [P1] *vs.* +1.68 (+1.74) e for U_{surf} and −1.65 (−1.67) e for N_{surf} obtained in analogous spin-polarized calculations [P4].

Model of system	E_{bind}, eV	q_O, e	$q_{U(1)}$, e	$q_{U(2)}$, e	$q_{U(3)}$, e	$q_{N(1)}$, e	$d_{O\text{-}U}$, Å	$\Delta z_{U(1)}$, Å	$\Delta z_{U(2)}$, Å	$\Delta z_{U(3)}$, Å	$\Delta z_{N(1)}$, Å
2 × 2, 5-layers, with frozen spin	6.9	-1.04	1.96	1.86	1.83	-1.60	1.91	+0.135[a]	-0.02	-0.04	-0.05
2 × 2, 5-layers	7.57	-1.08	2.09	1.82	1.84	-1.63	1.88	+0.16	+0.025	+0.003	-0.09
2 × 2, 7-layers	7.51	-1.08	2.19	1.78	1.78	-1.64	1.89	+0.17	+0.03	-0.02	-0.09
2 × 2, 7-layers, in proximity of N vacancy	7.58	-1.08	1.84	1.50	1.48	-1.61* -1.61^	1.88	+0.14	+0.01	-0.02	-0.09* -0.08^
3 × 3, 5-layers	7.59	-1.09	2.13	1.80	1.74	-1.62	1.88	+0.16	+0.01	-0.01	-0.10
3 × 3, 7-layers	7.57	-1.09	2.13	1.78	1.79	-1.62	1.88	+0.16	+0.01	-0.01	-0.09
3 × 3, 7-layers, in proximity of N vacancy	7.59	-1.09	1.86	1.47*	1.38*	-1.61* -1.61^	1.88	+0.10	-0.025*	-0.06*	-0.12* -0.11^
LCAO[b]	8.3	-0.89	1.97	1.66	1.62	-1.56	1.87	+0.15[b]	-0.07	-0.11	-0.04

[a] positive sign corresponds to atom displacement outward the substrate;
*, ^ adsorbed O atom in presence of non-equivalent N atomic neighbors for system containing N vacancy (Fig. 8.10a);
[b] LCAO calculations performed using *CRYSTAL-2006* code by group Prof. Evarestov.

Tables 8.1 and 8.2 clearly show that ionicity of O_{ads}–U_{surf} bond and effective atomic charges are slightly larger in spin-polarized calculations (this effect is less pronounced for O_{ads}–N_{surf}, we have obtained only slight increase of $|q_N|$). Relaxation shifts are also slightly larger in spin-relaxed calculations. The binding energy between adsorbed O and U/N

atoms is ~0.6-0.7 eV larger for spin-relaxed calculations as compared to the analogous spin-frozen calculations. If we estimate the binding energy of O adatom with defective surface in the proximity of N vacancy according to formula

$$E_{bind} = \frac{1}{2}\left(E^{\mathrm{UN(N\_vac)}} + 2E^{\mathrm{O_{triplet}}} - E^{\mathrm{O/UN(N\_vac)}}\right), \qquad \textit{(Eq. 8.1.2)}$$

where $E^{\mathrm{UN(N\_vac)}}$ is a total energy of defective UN substrate containing N vacancies while $E^{\mathrm{UN(N\_vac)}}$ the total energy of adsorbed oxygen atoms atop the defective substrate, the values calculated using Eqs. (*8.1.1* and *8.1.2*) are almost the same.

Table 8.2. The calculated parameters for O atom adsorbed atop the N_{surf} atom[a] (see caption and footnotes of Table 8.1 for explanation).

Model of system	E_{bind}, **eV**	q_O, e	$q_{N(1)}$, e	$q_{N(2)}$, e	$q_{N(3)}$, e	$q_{U(1)}$, e	$d_{O\text{-}N}$, Å	$\Delta z_{N(1)}$, Å	$\Delta z_{N(2)}$, Å	$\Delta z_{N(3)}$, Å	$\Delta z_{U(1)}$, Å
2 × 2, 5-layers, with frozen spin	5.0	-1.20	-1.44	-1.56	-1.59	1.805	2.19	-0.64	+0.065	+0.06	+0.10
2 × 2, 5-layers	5.52	-1.17	-1.48	-1.68	-1.68	1.86	2.19	-0.69	+0.03	+0.05	+0.13
2 × 2, 7-layers	5.58	-1.17	-1.48	-1.63	-1.67	1.86	2.21	-0.715	+0.03	+0.03	+0.12
3 × 3, 5-layers	5.57	-1.18	-1.51	-1.67	-1.68	1.89	2.20	-0.70	+0.01	+0.01	+0.13
3 × 3, 7-layers	5.65	-1.18	-1.51	-1.69	-1.65	1.89	2.22	-0.73	+0.01	+0.02	+0.12

[a] atomic positions of U and N ions are reversed as compared to those shown in Fig. 8.3.

8.1.4. Analysis of electronic properties

Electron density redistributions caused by the absorption of O atom atop N_{surf} or U_{surf} atoms on UN(001) surface in spin-relaxed case are shown in Fig. 8.4. An analysis of the difference density plots for both configurations of O_{ads} confirms that the oxygen adatom forms a strong bonding with the U_{surf} atom which can be considered as one-center adsorption complex (Fig. 8.4c, 8.4d). In the case of O adatom atop the N_{surf} atom, this is rather multi-center adsorption complex involving four adjacent surface U atoms (Fig. 8.4a, 8.4b). As follows from Table 8.2., these surface atoms mostly contribute to the high O binding energy atop the N_{surf}. Formation of the strong chemical bonding of O atom with the U_{surf} results in a strong anisotropic redistribution of the electronic charges, thus, indicating considerable contribution of uranium *f* and *d* electrons to chemical bonding. Plots of electron density redistributions clearly show that U_{surf} atoms shield influence of neighbor atoms on the next coordination spheres much better than N_{surf} atoms. When using 7-layers 3 × 3 supercells, we can avoid the effect of finite-slab size.

Adsorption of O_{ads} atop the surface N or U atoms on the UN(001) surface leads to appearance of the specific oxygen bands in the density of states (DOS) (Fig. 8.5) as compared to DOS for a pure UN(001) surface (Fig. 6.2). For oxygen atop the U_{surf}, O(*2p*) states overlap with the U_{surf}(*6d*) and with a well-pronounced tail of U_{surf}(*5f*) states in the region of the N_{surf} (*2p*) valence band (-2 to -4 eV). This indicates once more a strong oxygen chemical bonding (chemisorption) with U_{surf} typical for metal surfaces. However,

when O is located atop N_{surf}, the contribution from $U_{surf}(5f)$ state in this energy region diminishes whereas $N_{surf}(2p)$ states are noticeably pushed down to smaller energies, due to N_{surf} atom repulsion from negatively charged O adatom.

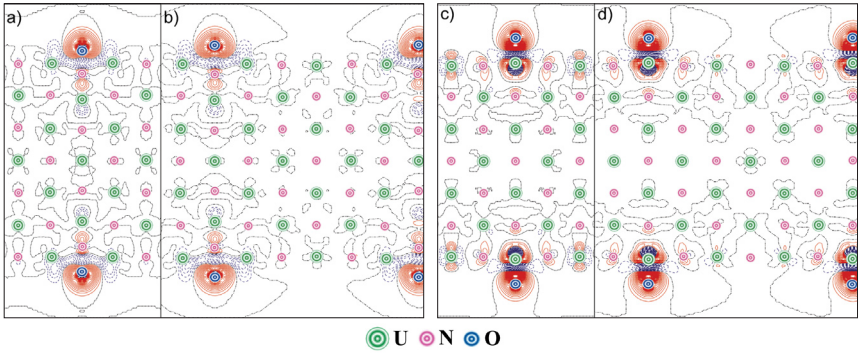

Figure 8.4. The 2D sections of the electron charge density re-distributions $\Delta\rho(\mathbf{r})$ for O atoms adsorbed atop (*i*) N_{surf} atom for 2 × 2 (a) and 3 × 3 (b) supercells as well as (*ii*) U_{surf} atom for 2 × 2 (c) and 3 × 3 (d) supercells upon the seven-layer UN(001) slab. Function $\Delta\rho(\mathbf{r})$ is defined as the total electron density of the interface containing adsorbed O atom minus the densities of substrate and adsorbate with optimized interfacial geometry. Solid (red) and dashed (blue) isolines correspond to positive and negative electron densities, respectively. Dot-dashed black isolines correspond to the zero-level.

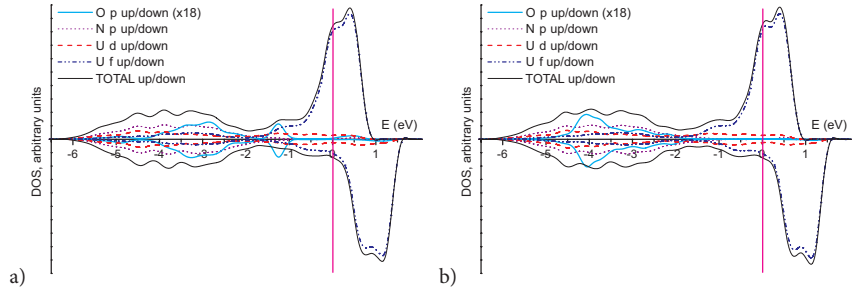

Figure 8.5. The total and projected DOS for O atoms distributed with 3 × 3 periodicity atop 7–layer UN(001) slab: a) adsorpion atop N atom, b) adsorpion atop U atom. A convolution of individual energy levels has been plotted using the Gaussian functions with a half-width of 0.2 eV.

8.1.5. Comparison of oxygen adsorbtion upon UN(001) and UN(110) surfaces

We have also estimated the binding energies of oxygen adatom with UN(110) surface (Table 8.3). We have found these results qualitatively similar to those for O adsorption

on (001) surface. For both surfaces, oxygen binding energy with U atom is larger as compared to that with N atom (~1.9 eV for (001) and ~2.1–2.2 eV for (110) surface). Moreover, increase of the surface supercell from 2 × 2 to 3 × 3 leads to slight growth of binding energy. Oxygen binding energies on (110) surface are ~0.1-0.4 eV larger as compared to (001) surface. Higher E_{bind} values for (110) surface can be explained by larger distances between surface adatoms upon (110) surface resulting in decreased interactions between adsorbed oxygen and all other atoms, excluding underlying U or N atom.

Table 8.3. The calculated binding energies ($E_{bind,}$ eV) for oxygen adsorption atop UN (001) and (110) surfaces.

Number of layers and supercell size		Atop U	Atop N
		Binding energy, eV	Binding energy, eV
(001)	7, 2 × 2	7.51	5.58
	7, 3 × 3	7.57	5.65
(110)	7, 2 × 2	7.90	5.73
	7, 3 × 3	7.91	5.99

8.1.6. Atomic oxygen adsorption: Summary

Summing up, the results presented in subsection 8.1 for single oxygen atom interaction with UN surfaces demonstrate strong chemisorption typical for metallic surfaces. The excellent qualitative agreement of the results obtained using the two different first principles methods supports their reliability for simulations on O/UN interface. O adatom atop U_{surf} atom forms the one-center complex with underlying U_{surf} atom, while oxygen adsorption atop N_{surf} leads to formation of complex containing the four adjacent U_{surf} atoms.

8.2. Molecular oxygen adsorption

8.2.1. Model and theoretical background

The results analyzed in Section 8.1 and Ref. [P2] clearly demonstrate the metallic nature of UN surface. In this subsection, we simulate the interaction of *molecular* oxygen with the perfect UN(001) surface [P3]. The key questions arisen here are: whether the O_2 dissociation upon the surface is energetically possible, which adsorption sites are optimal for this, and whether it can occur spontaneously, without energy barrier, similarly to other metallic surfaces, for example Al [79].

Calculations on molecular adsorption have been performed using the fixed total spin equals to 1 μ_B on each U atom. For simulation on the chemisorption of oxygen molecule, we have used the 5-layer 2 × 2 extended surface supercell (containing 20 U and 20 N atoms). The periodic adsorbate distribution corresponds to the molecular coverage of 0.25 ML (or atomic O coverage of 0.5 ML). To reduce computational efforts, we have used a symmetric two-sided arrangement of oxygen molecules again. The binding energy E_{bind} *per* oxygen atom in the adsorbed molecule $(O_2)_{ads}$ was calculated as:

$$E_{bind} = \frac{1}{4}\left(E^{\mathrm{UN}} + 2E^{\mathrm{O_2}} - E^{\mathrm{O_2/UN}}\right), \qquad \textit{Eq. (8.2.1)}$$

where $E^{\mathrm{O_2/UN}}$ is the total energy of a fully relaxed O_2/UN(001) slab for several configurations of (O_2) upon the substrate (with a center of molecule atop the corresponding surface site as shown in Fig. 8.7), $E^{\mathrm{O_2}}$ and E^{UN} the total energies of an isolated oxygen molecule in the ground (triplet) state and of a relaxed UN slab, respectively. The factor 1/4 before brackets, similar to atomic adsorbtion calculations, appears since the substrate is modeled by a slab containing the two equivalent surfaces with $(O_2)_{ads}$ positioned symmetrically relatively to slab surfaces whereas each molecule before and after dissociation contains two O atoms. When modeling the molecular adsorption, we have analyzed different configurations of O_2 molecule in the triplet state on the UN(001) substrate. *Vertical* orientations of the molecule atop the surface N or U ions have been found to be metastable with respect to molecule reorientation to the *horizontal* configuration, parallel to the surface. We have estimated both the binding energy of a molecule, using Eq. (8.2.1), and the dissociation energy of molecule (for some configurations), *i.e.,* the difference of the total energies of a slab with an O_2 molecule before and after dissociation, when the two O atoms in the triplet state are positioned atop the two nearest U_{surf} atoms (Table 8.4).

8.2.2. Spontaneous dissociation

We have found that a spontaneous, barrierless O_2 dissociation takes place in the two cases: when the molecular center is atop either (*i*) a hollow site or (*ii*) N_{surf} atom, with the molecular bond directed towards the two nearest U_{surf} atoms (the configurations 1 and 5 in Fig. 8.6, respectively). The relevant dissociation energies E_{diss} are given in Table 8.4, along with other parameters characterizing the atomic relaxation and the Bader charge distribution. Geometry and charges for the configurations 1 and 5 after dissociation (Table 8.4) are qualitatively similar to those obtained for UN(001) substrate covered by chemisorbed O atoms, *e.g.*, U_{surf} atoms beneath the oxygen adatom after dissociation are shifted up in both configurations (Table 8.4). However, since concentration of O_{ads} in these calculations is twice as larger as compared to that for atomic oxygen adsorbtion [P2, subsection 8.1], some quantitative differences of the results presented in Tables 8.4 and 8.1 for oxygen atom adsorbtion atop U_{surf} atom are unavoidable. For example, the *repulsion* energy between the two adatoms after O_2 dissociation, which are positioned atop the two nearest U_{surf} atoms (the configuration 1) is quite noticeable, ~0.7 eV.

We have also identified two other configurations of adsorbed oxygen molecules where the dissociation is energetically possible with energy barrier: (*i*) atop the hollow site when a molecular bond is oriented towards the nearest N_{surf} atoms (the configuration 2 in Fig. 8.6) and (*ii*) atop the U_{surf} atom (for any molecular orientation, *e.g.*, the configurations 3 and 4 in Fig. 8.6). For the configuration 2, we have observed the orientation instability of the adsorbed molecule which easily rotates, *e.g.*, towards the U_{surf} atom with further dissociation. The configurations 3 and 4 rather describe metastable UO_2 *quasi-molecules*, due to a strong bonding between all three atoms (Fig. 8.7c) and since the corresponding U_{surf} atom is noticeably shifted up from its initial positions on surface (Table 8.4). The dissociation of $(O_2)_{ads}$ molecule in configuration 3 is energetically possible but only after overcoming the activation energy barrier.

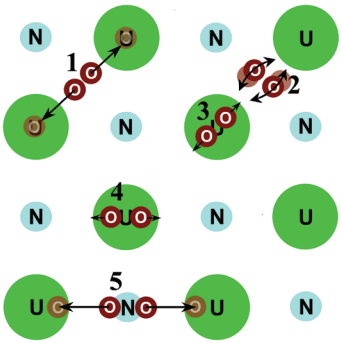

Figure 8.6.
Schematic view of five different horizontal configurations for the O_2 molecule adsorption on UN surface: 1) atop the hollow site oriented towards the nearest U_{surf} atoms, 2) atop the hollow site oriented towards the nearest N_{surf} atoms, 3) atop the U_{surf} atoms oriented towards the next-nearest surface U_{surf} atoms, 4) atop the U_{surf} atoms oriented towards the nearest N_{surf} atoms, 5) atop the N_{surf} atoms oriented towards the nearest U_{surf} atoms. We show that spontaneous dissociation of molecule can occur when O_2 is located either atop the hollow site (1) or atop the N_{surf} atom (5).

Table 8.4. The calculated values of binding (E_{bind}, Eq. (8.2.1)) and dissociation (E_{diss}) energies, geometry (z, Δz) and Bader charges (q) for configurations of molecular and spontaneous dissociative chemisorption of oxygen molecule upon the UN(001) substrate. Numbers in brackets correspond to the configurations shown in Fig. 8.6. The calculated binding energy for a free O_2 molecule in the triplet state is 6.06 eV and a bond length is 1.31 Å (*cf.* with experimental values of 5.12 eV and 1.21 Å, respectively) [81].

Position		E_{bind} per O atom, eV	z[a], Å	E_{diss}, eV	q(O), e	q(U1[b]), e	q(U2[c]), e	q(N[d]), e	Δz[e](U1), Å	Δz[e](U2), Å	Δz[e](N), Å
hollow (1)	molecular adsorption	3.03	1.893	-	-0.465	1.913	1.762	-1.533	-0.050	-0.050	0.025
	after dissociation	6.04	1.957	3.01	-0.978	2.053	1.978	-1.577	0.075	0.068	-0.133
atop U	towards next-nearest U (3)	4.00	2.18	-	-0.5905	2.042	1.836	-1.6065	0.176	-0.048	-0.096
	towards nearest N (4)	4.18	2.14	-	-0.578	2.0485	1.827	-1.625	0.123	-0.051	-0.106
atop N (5)	molecular adsorption	2.67	2.020	-	-0.5685	1.8675	1.832	-1.354	-0.050	-0.050	0.025
	after dissociation	5.85	1.955	3.18	-0.979	2.115	1.876	-1.580	0.073	0.021	-0.201

[a] z is the height of O atoms respectively the non-relaxed UN substrate,
[b] U1 the nearest surface U_{surf} atom,
[c] U2 the next-nearest U_{surf} atom,
[d] N the nearest N_{surf} atom,
[e] Δz the additional vertical shifts of the same surface atoms from their positions in absence of adsorbed oxygen.

8.2.3. Electronic properties of adsorbed molecule

Adsorption of an O_2 molecule (in the triplet state) is accompanied by the charge transfer of ~1 e (*per* molecule) from the substrate (Table 8.4). In Fig. 8.7, we analyze the difference electron charge redistributions for three configurations of horizontally

oriented $(O_2)_{ads}$ molecules upon the surface: (*a*) molecule adsorbed upon the hollow site (the configuration 1, Fig. 8.6), (*b*) molecule dissociated from this configuration with O adatoms located atop the nearest U_{surf} atoms, and (*c*) molecule adsorbed upon the U_{surf} atom (at configuration 3). Spontaneous O_2 dissociation and, thus, a smooth transition from the charge distribution (a) to (b) can be explained by continuous areas of the electron density (Fig. 8.7a) parallel to the surface which may be considered as *dissociation channels*, analogously to the density plot for a molecular oxygen upon the Al substrate [79].

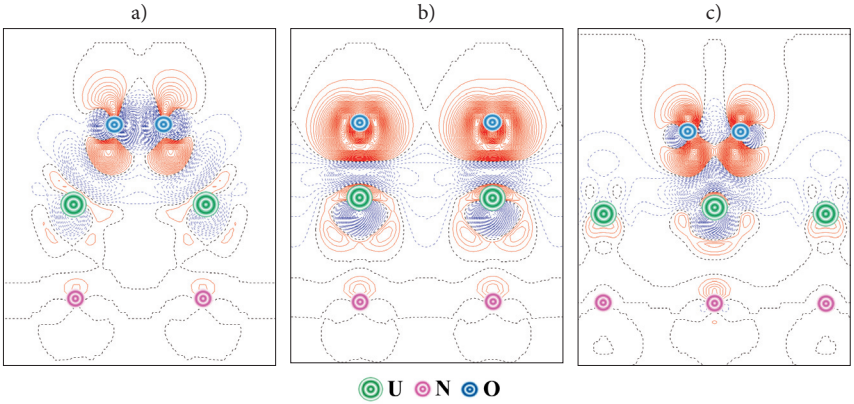

Figure 8.7. The difference electron density maps $\Delta\rho(\mathbf{r})$ (the total density of the interface minus the sum of densities of substrate and adsorbate with optimized interfacial geometry) (a) for the O_2 molecule upon the hollow position oriented to the nearest U_{surf} atoms, (b) after its dissociation in the configuration 1 (Fig. 8.6) with O atoms atop the U_{surf} atoms and (c) for the O_2 molecule atop the U_{surf} atom in the configuration 3 (Fig. 8.6). Solid (red) and dashed (blue) isolines correspond to positive and negative electron density, respectively. Isodensity increment is 0.003 e Å^{-3}.

After dissociation, each O adatom contains an extra charge of ~1 *e*, *i.e.,* transforms into O^- ion in the triplet state (Fig. 8.7b). In contrast, when considering the molecular configuration 3, these *dissociation channels* are transformed into *dissociation barriers* (Fig. 8.7c). Simultaneously, we observe considerably higher electron density, indicating a kind of UO_2 quasi-molecule with a strong bonding between the O_2 molecule and surface U atom beneath. Thus, difference between the electron density plots presented in Figs. 8.7a and 8.7c can explain different dissociation abilities of O_2 molecule in the configurations 1 and 3 (Fig. 8.6).

For the same adsorbate configurations considered above, we have constructed the total and projected densities of states (DOS) (Fig. 8.8). Molecular adsorption in these configurations leads to appearance of the specific *oxygen bands* as compared to those for oxygen adatoms upon UN surface (Fig. 8.5) and O atom substituted for a host N atom in UN bulk [82]. For a molecular oxygen atop the hollow position (Fig. 8.6a), O(*2p*) peak

is observed at -1 eV overlapping with the U(*5f*) and U(*6d*) bands. After O_2 dissociation (Fig. 8.7b) this peak disappears being replaced by the broad two-peak band in the region of the N(*2p*) valence band (from -2 to -5 eV), similarly to the DOS for oxygen adatoms on UN(001) substrate (Fig.8.5). Some differences are also noticeable between the corresponding U *5f* and *6d* peaks in the spectral range above -1 eV (Figs. 8.8a-8.8c) which can be caused by both different arrangement of O and U atoms in these configurations and sensitivity of U states to the presence of oxygen, thus indicating a strong oxygen chemical bonding (chemisorption). When oxygen molecule is located atop the U_{surf} atom (the configuration 3), the U(5*f*) and U(6*d*) contributions in the energy range above -1 eV are diminished, simultaneously the O(*2p*) contribution grows, thus increasing an overlap between all three states and indicating UO_2 quasi-molecular bond formation. As compared to the adsorption of oxygen molecule upon the hollow site (Fig. 8.8a), we again observe a higher O(*2p*) peak (at -1.5 eV) and an additional lower peak of the same O(*2p*) (at -5.5 eV) which noticeably overlaps with the U(*5f*) and U(*6d*) subpeaks (Fig. 8.8c). Some analogue of the latter pattern was observed earlier for the projected DOS of O atom substituted for N atom in UN bulk [82]. In all three DOSs (Fig. 8.8), a broad band containing the N(*2p*) projected states is not changed drastically which means a weak influence of N atoms on the O_2 molecule adsorption upon the UN(001) surface.

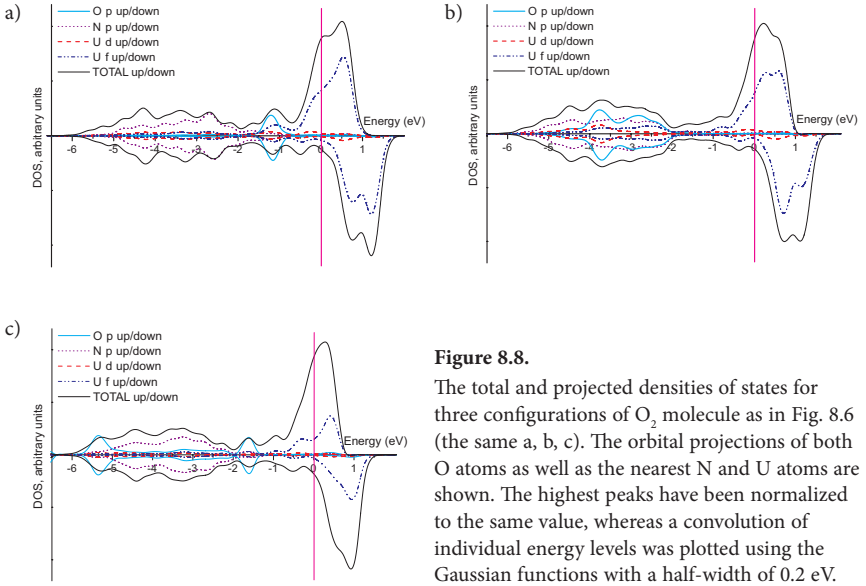

Figure 8.8.
The total and projected densities of states for three configurations of O_2 molecule as in Fig. 8.6 (the same a, b, c). The orbital projections of both O atoms as well as the nearest N and U atoms are shown. The highest peaks have been normalized to the same value, whereas a convolution of individual energy levels was plotted using the Gaussian functions with a half-width of 0.2 eV.

Summing up, the results of *ab initio* calculations on adsorption of oxygen molecule upon the perfect UN(001) surface clearly demonstrate a real possibility for spontaneous dissociation of the adsorbed oxygen, analogously to the O_2 dissociation on "traditional" metallic surfaces.

8.3. Simulation of migration path for O adatom along the UN(001) surface

We have considered three main migration paths of oxygen adatom upon the UN(001) surface (Fig. 8.9): (*i*) path 1: between the sites atop U_{surf} atom and the nearest N_{surf} atom, (*ii*) path 2: between the sites atop the two neighboring U_{surf} atoms, (*iii*) path 3: between the sites atop the two neighboring N_{surf} atoms:

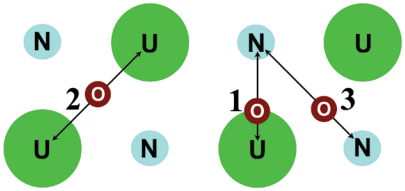

Figure 8.9. Different oxygen migration paths upon the UN(001) surface (atop view).

Table 8.5. Binding energies E_{bind} of adsorbed oxygen in different positions atop UN slab (Fig. 8.9).

1. From site atop U_{surf} to site atop N_{surf} (migration path 1)				
Supercell size:	2 × 2		3 × 3	
Number of atomic layers:	5	7	5	7
atop U_{surf}	7.57	7.51	7.59	7.57
¼ of distance U-N (or 0.61 Å from U atom)	7.39	7.39	-	-
½ of distance U-N (or 1.22 Å from U atom)	6.97	6.98	-	-
¾ of distance U-N (or 1.83 Å from U atom)	5.91	5.93	-	-
atop N_{surf} (or 2.43 Å from U atom)	5.52	5.58	5.57	5.65
2. From hollow position (h.p.) to site atop U_{surf} (migration path 2)				
Supercell size:	2 × 2		3 × 3	
Number of atomic layers:	5	7	5	7
atop h.p.	7.21	7.245	7.20	7.21
¼ of distance h.p.-U (or 0.43 Å from h.p.)	7.23	7.255	-	-
½ of distance h.p.-U (or 0.86 Å from h.p.)	7.32	7.33	-	-
¾ of distance h.p.-U (or 1.29 Å from h.p.)	7.45	7.45	-	-
atop U_{surf} (or 1.72 Å from h.p.)	7.57	7.51	7.59	7.57
3. From hollow position (h.p.) to site atop N_{surf} (migration path 3)				
Supercell size:	2 × 2		3 × 3	
Number of atomic layers:	5	7	5	7
atop h.p.	7.21	7.25	7.20	7.21
1/4 of distance h.p.-N (or 0.43 Å from h.p.)	6.61	6.65	-	-
1/2 of distance h.p.-N(or 0.86 Å from h.p.)	6.32	6.35	-	-
3/4 of distance h.p.-N(or 1.29 Å from h.p.)	5.54	5.57	-	-
atop N_{surf} (or 1.72 Å from h.p.)	5.52	5.58	5.57	5.65

The binding energy E_{bind} of oxygen atom adsorbed upon the UN surface has been defined in subsection 8.1.1. To reduce the computational time for calculations on oxygen adatom in interstitial positions, we have relaxed only z coordinates of slab atoms fixing their x and y coordinates. For adsorption of O atoms atop the N_{surf} or U_{surf} atoms, the total slab geometry relaxation has been performed, to control changes of symmetry arisen due to lateral interaction. The results obtained for all migration paths of adatom for different slab thicknesses and supercell extensions are systematized in Table 8.5. This Table presents the values of binding energies calculated for migration paths of O adatoms upon the perfect UN(001) substrate shown in Fig. 8.9. We have fixed five sites along the O_{ads} migration trajectories for 2×2 supercells of UN(001) slab and two sites for 3×3 supercells. In both cases, the most favorable migration trajectory has been optimized to be the line joining the sites atop the nearest surface U atoms and the hollow sites between them (trajectory 2). The corresponding energy barriers found to be 0.36 eV (5-layer slab) and 0.26 eV (7-layer slab) indicates on a high mobility of O_{ads} atoms upon UN. The energy barriers along other two migration trajectories are substantially larger (1.93-2.05 eV and 1.31-1.69 eV for trajectories 1 and 3, Fig. 8.9).

Thus, we observe quite high mobility of atoms along the surface, due to relatively low migration barriers.

9. O atom migration and incorporation into defective UN(001) slab

9.1. Low-barrier incorporation of O adatom from site atop U_{surf} atom to N_{surf} vacancy

To understand the initial mechanism of adatom incorporation into the surface layer of UN(001), it is necessary to clarify both energetic and structural possibilities of O_{ads} migration along this substrate, both perfect and defective. To estimate oxygen adatom mobility upon the UN(001) surface, we have performed a series of *ab initio* spin-polarized calculations.

According to our calculations, O atom adsorbed atop the U_{surf} atom in the proximity of the surface N vacancy can be captured by the latter (Fig. 9.1) when overcoming a low energy barrier (~0.5-1 eV). We have estimated the energy gain for such a transition of oxygen adatom using the formula:

$$\Delta E = \frac{1}{2}\left(E_{tot}^{\mathrm{UN(O\_in\_N\_vac)}} - E_{tot}^{\mathrm{UN(O\_atop\_U)}}\right), \qquad \textit{Eq. (9.1.1)}$$

where $E_{tot}^{\mathrm{UN(O\_in\_N\_vac)}}$ is the total energy of the supercell containing the O atom in the N vacancy (position 2 as shown in Fig. 9.1), and $E_{tot}^{\mathrm{UN(O\_atop\_U)}}$ the total energy of the supercell with O atom adsorbed atop U_{surf} atom positioned in the proximity of existing N vacancy (position 1). For calculations on $E_{tot}^{\mathrm{O/UN(N\_vac)}}$, we have fixed horizontal *x* and *y* oxygen coordinates, to prevent O adatom migration. Multiplier ½ in Eq. (9.1.1) appears due to the symmetric arrangement of adsorbed or incorporated O atoms. When comparing $E_{tot}^{\mathrm{UN(O\_in\_N\_vac)}}$ value (obtained as a result of adatom migration from position atop U_{surf} atom into vacancy) with $E_{tot}^{\mathrm{UN(O\_in\_N\_vac)}}$ where O adatom is directly incorporated into pre-existing vacancy (Section 9.2) the corresponding difference does not exceed 0.01 eV. The calculated energy gain (ΔE_g) for the transition from position 1 to position 2 (as shown in Fig. 9.1) equals to ~2 eV *per* oxygen adatom (1.99 eV for 2 × 2 7-layer supercell and 1.94 eV for 3 × 3 7-layer supersell).

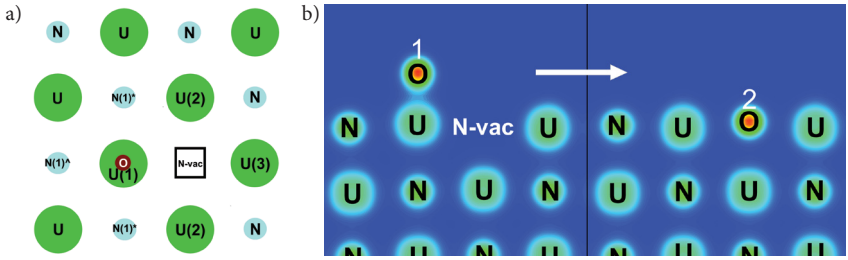

Figure 9.1. Atop (a) and across (b) views of surface model used for simulation of oxygen atom low-barrier incorporation from the initial position (1) atop U_{surf} atom (left) into the nearest existing N_{surf} vacancy (2). Numbers enumerate non-equivalent surface atoms for oxygen adsortion in proximity of N_{surf} vacancy (see caption of Fig. 8.3).

In Fig. 9.2, the diference of electron charge redistributions for oxygen adsorpion atop U_{surf} atom in the proximity of the surface N vacancy is analyzed. The electron charge redistributions in the slab look similarly to adsobtion atop U_{surf} atom without adjacent N vacancy (Fig. 8.4c,d). Parallel to the surface between adsorbed O atom and existing N vacancy the electrostatic channels with electronic density shortage can be observed which are directed towards the oxygen adatom incorporation into the N vacancy.

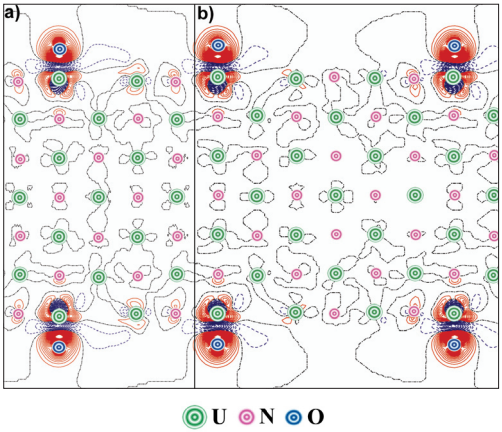

Figure 9.2. The 2D sections of the electron charge density re-distributions $\Delta\rho(\mathbf{r})$ for O atoms adsorbed atop U_{surf} atom near the surface N vacancy. Other details are given in caption of Figure 8.4.

Thus, we have showed the possibility of low-barrier oxygen adatom incorporation into existing N vacancy from the nearest adsorption site atop U_{surf} atom.

9.2. Oxygen incorporation into surface vacancies

9.2.1. Model and computational details

One of possible ways for UN surface oxidation is the formation of oxynitrides near the UN surface [18]. Hence, it is very impotant to describe the oxygen interaction with the single vacancies. As known from literature, considerable attention was paid so far for the static and dynamic properties of primary defects (vacancies and incorporated impurities) in UN *bulk* [34] which affect the fuel performance during operation and its reprocessing. Apart the behavior of empty vacancies, the O atom incorporation into vacancies in bulk UN has been considered too. Incorporation of oxygen atom into the N vacancy in bulk has been found to be energetically more favorable as compared to the interstitial sites [82]. However, the solution energy shows an opposite effect. In order to shed more light on the mechanism of unwanted UN oxidation, the incorporation of oxygen impurities into the N- and U- vacancies on the UN(001) surface is focused in this subsection and Ref. [P5].

Our calculations have been performed for the supercells with 2×2 and 3×3 extensions of translation vector upon the UN surface. Oxygen-occupied N and U vacancies have been disposed in the surface, subsurface and central layers of 2D slab. Due to the presence of mirror layers in the symmetric slabs, one can consider the two-sided symmetric arrangement of defects, except for the central mirror plane, thus, minimizing the computational expenses. The spin magnetic moment was allowed to relax in all the calculations for the FM spin arrangements on the uranium sublattice.

9.2.2. Oxygen incorporation and solution energies

The energy balance for the incorporation of an O atom into a vacancy can be characterized by *the incorporation energy* E_I suggested by Grimes and Catlow [83] in the shell model calculations on fission products in UO_2:

$$E_I = E^{\mathrm{UN(O\_}inc\mathrm{)}} - E^{\mathrm{UN(N/U\_vac)}} - E^O, \qquad \textit{Eq. (9.2.1a)}$$

for the O atom incorporated into the N- and U vacancy disposed in the central atomic layer and

$$E_I = \frac{1}{2}(E^{\mathrm{UN(O\_}inc\mathrm{)}} - E^{\mathrm{UN(N/U\_vac)}} - 2E^O), \qquad \textit{Eq. (9.2.1b)}$$

for the same incorporation in the surface or sub-surface layers. Here $E^{\mathrm{UN(O\_}inc\mathrm{)}}$ is the total energy of the supercell containing the O atom at either the N- or U vacancy ($E^{\mathrm{UN(O\_}inc\mathrm{)}} < 0$), $E^{\mathrm{UN(N/U\_vac)}}$ the energy of the supercell containing an unoccupied (empty) vacancy, and E^O half the total energy of isolated O_2 molecule in the triplet state. It is defined by the oxygen chemical potential at 0 K. Since the value of E_I describes the energy balance for the incorporation into pre-existing vacancies, it has to be negative for energetically favorable incorporation processes.

To take into account the total energy balance, including the vacancy formation energy E_{form} in the defect-free slab, the solution energy [83] has been defined as:

$$E_S = E_I + E_{form}, \qquad \textit{Eq. (9.2.2)}$$

where E_{form} is the formation energy of N- or U vacancy in the slab calculated using *Eq.7.1.1a* or *7.1.1b.*

It is worth mentioning, however, that use of the standard O pseudopotential in our *VASP* calculations gave good bond length of 1.23 Å for the O_2 molecule but considerable overestimated its binding energy (6.79 eV *vs.* the experimental value of 5.12 eV). Several corrections were suggested in the literature how to take into account this serious DFT shortcoming [84, 85]. Thus, the calculated formation and solution energies of defect may be corrected by ~1 eV (its impact is discussed below).

Table 9.1. Incorporation (E_I) and solution (E_S) energies (eV), average spin magnetic moments of U atoms μ_{av}^{U} (μ_B) as well as effective charge of oxygen atoms (e^-) for O incorporation into the UN(001) surface. The reference states for calculation of the incorporation and solution energies have been chosen as the chemical potentials of O, N and U calculated for O_2, N_2 molecules and α-U, respectively.

Layer	Supercell size	Number of atomic layers in slab	N vacancy				U vacancy			
			E_I (eV)	E_S (eV)	μ_{av}^{U} (μ_B)	$q_{eff}(e^-)$	E_I (eV)	E_S (eV)	μ_{av}^{U} (μ_B)	$q_{eff}(e^-)$
Surface	2 × 2	5	-6.173	-2.473	1.65	-1.36	-0.339	1.120	1.16	-0.98
		7	-6.181	-2.476	1.49	-1.36	-0.855	0.583	1.36	-1.03
		9	-6.188	-2.479	1.41	-1.36	-0.943	0.493	1.31	-1.06
	3 × 3	5	-6.122	-2.481	1.60	-1.37	-0.683	0.654	1.48	-1.05
		7	-6.126	-2.480	1.46	-1.36	-1.073	0.230	1.38	-1.08
Subsurface	2 × 2	5	-6.314	-2.068	1.64	-1.42	-1.856	1.284	1.66	-1.10
		7	-6.419	-2.090	1.49	-1.40	-1.823	1.297	1.45	-1.10
		9	-6.417	-2.091	1.41	-1.40	-1.823	1.271	1.38	-1.10
	3 × 3	7	-6.428	-2.093	1.46	-1.39	-2.012	1.000	1.43	-1.10
Central (mirror)	2 × 2	7	-6.611	-2.180	1.47	-1.42	0.736	3.923	1.44	-0.89
		9	-6.608	-2.192	1.39	-1.38	0.669	3.838	1.38	-0.90
	3 × 3	7	-6.599	-2.182	1.45	-1.42	0.317	3.378	1.47	-0.94

The calculated O adatom incorporation into the N vacancy at the UN(001) surface has been found to be energetically favorable since both values of E_I and E_S are strictly negative (Table 9.1). This is in favor of both creation of the N vacancy and adsorption of the O atom from air. Also, E_I decreases by ~0.4 eV (becomes more negative) within the slab as compared to the surface layer, whereas E_S is smallest for the N vacancy just on the surface layer. In contrary, in the case of U vacancies, the values of E_I calculated for the surface and central layers have been found to be close to zero. The sub-surface layer is characterized by E_I which is ~1 eV smaller than that for the surface and central layers. Our results indicate importance of oxynitride formation. However, E_S is positive and increases for O atoms in the the U vacancy and the slab center. The energies in Table 9.1 do not include the corrections discussed above for the O atoms. However, such corrections may lead to E_I (or E_S) increased by ~1 eV and, as a result, more positive E_I for the U vacancy. Table 9.1 also indicates that solution of the oxygen atoms is energetically more favorable at the surface layers than inside the slab. As the supercell size increases (the 3 × 3 extension in Table 9.1), both E_I and E_S values decrease whereas influence of the slab thickness is not so clear. Nevertheless, the U vacancy appeared to be most sensitive to the supercell size related to spurious interactions between the periodically repeated defects. The E_I as well as E_S values may be reduced by 0.15 eV at the average in this case.

9.2.3. Spin densities and Bader charges

Table 9.1 allows us to analyze also the averaged spin density of U atoms (μ_{av}^{U}) for different morphologies of defective UN(001) surfaces with incorporated O atoms. Analogously to defective UN surface with empty vacancies [P4], μ_{av}^{U} decreases with

a number of layers in the slab for both types of the vacancies (except for the O atom incorporated into the U vacancy in the surface layer). It is also seen that μ_{av}^{U} is higher in the surface layer for the N vacancy than for the U vacancy. The sub-surface and central layers are characterized by similar μ_{av}^{U} for both types of vacancies. Interestingly, the effective charge q_{eff} on O atoms is also higher for the N vacancy and inside the slab. However, in the case of U vacancy, q_{eff} decreases by almost 0.3 *e*. The same effect has been also observed for adjacent N atoms: their effective charge is smaller when the O atom occupies the U vacancy. The overall picture suggests prevalence of the covalent bonding between different species in the system.

9.2.4. Charge redistribution analysis: Finite-size effects and choice of supercell size

Large concentrations of defects (25% for the 2 × 2 extension in Table 9.1) causes certain finite-size effects which can be illustrated using the 2D difference electron density redistributions $\Delta\rho(\mathbf{r})$. These plots are shown for the O atoms incorporated into the N vacancies at the surface (Fig. 9.3) and central layers (Fig. 9.4). Inside the 5-layer slab, a presence of the two symmetrically positioned defects induces their interaction (visible in charge redistribution across a slab in Fig. 9.3a). An increase of the slab thickness reduces this effect (Fig. 9.3c). If the supercell size is decreased (the 2 × 2 extension, Fig. 9.3b) an additional electron density parallel to the surface layer is observed between the defects. Similar effects are also observed for redistributions of the electron density around defects in the mirror planes (Fig. 9.4). The effect of supercell size in this case is similar to that discussed for the N vacancy.

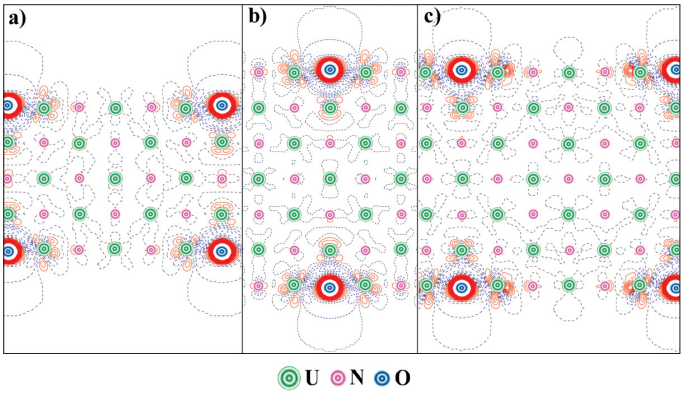

Figure 9.3. The 2D sections of the electron charge density re-distributions $\Delta\rho(\mathbf{r})$ around the O atoms incorporated into the surface N vacancies of the 5- and 7-layer UN(001) slabs with 2 × 2 and 3 × 3 supercell extensions. $\Delta\rho(\mathbf{r})$ are defined as the total electron density of the O-containing defected surface minus a superposition of the electron densities of the surface containing the N vacancies and the O atom in the regular positions on the surface. a) 3 × 3 periodicity of the O atoms upon the five-layer slab, b) 2 × 2 periodicity of the O atoms upon the seven-layer slab, c) 3 × 3 periodicity of the O atoms upon the seven-layer slab. Other details are given in caption of Figure 8.4.

The effect of supercell size in this case is similar to that discussed for the N vacancy. However, in the case of surface U vacancy, a larger concentration of electron density was seen between the O atom and neighbouring N atoms in the sub-surface layer, in a comparison to the N vacancy. Thus, the effect of slab thickness also may not be underestimated in this case.

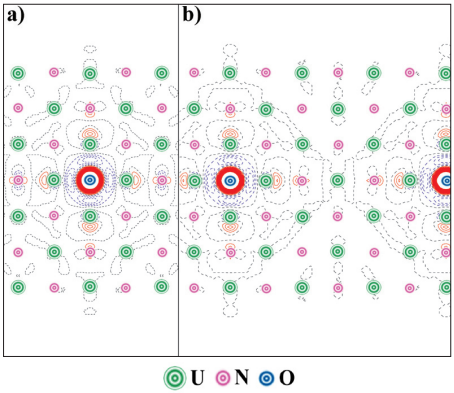

Figure 9.4. The 2D sections of $\Delta\rho(\mathbf{r})$ around the O atoms incorporated into the N vacancies in central layer of 7-layer UN(001) slabs with (a) 2 × 2 and (b) 3 × 3 supercell extensions. Other details are given in caption of Figure 9.3.

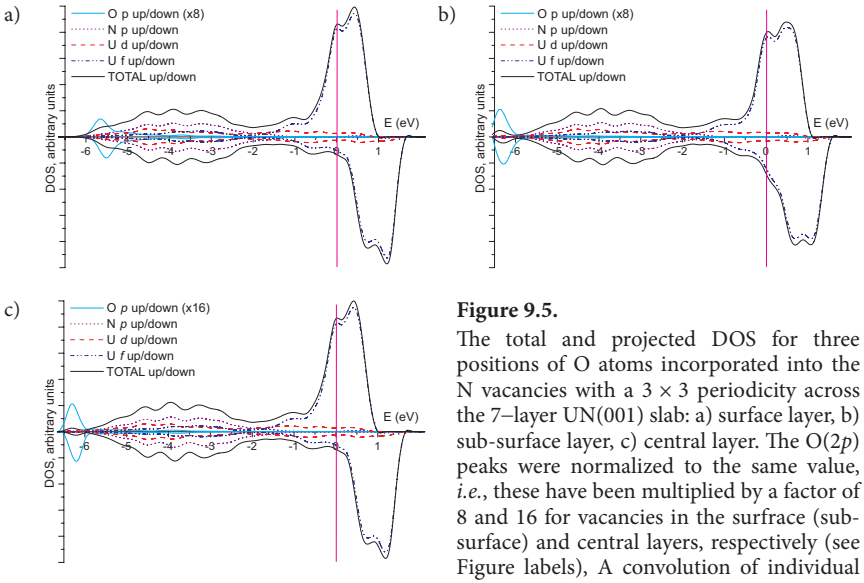

Figure 9.5.
The total and projected DOS for three positions of O atoms incorporated into the N vacancies with a 3 × 3 periodicity across the 7–layer UN(001) slab: a) surface layer, b) sub-surface layer, c) central layer. The O(2*p*) peaks were normalized to the same value, *i.e.*, these have been multiplied by a factor of 8 and 16 for vacancies in the surface (sub-surface) and central layers, respectively (see Figure labels), A convolution of individual energy levels was plotted using the Gaussian functions with a half-width of 0.2 eV.

9.2.5. *Electronic densities of states (DOS) for incorporated oxygen*

In Figure 9.5, the total and projected densities of states are shown for the 7-layer defective UN(001) surface with the O atom incorporated into the N vacancy. The system remains conducting throughout all the calculations with the significant contribution from the U(*5f*) states at the Fermi level similar to perfect UN(001) slab (Fig. 6.2). The appearance of specific O(2*p*) band with the energy peak at –6 eV is observed. When comparing the DOS for the O atoms incorporated into the N vacancies, a noticeable shift of the O(*2p*) band (by about -1.0 eV) allows one to distinguish the surface layer from the internal layers.

Moreover, in the case of surface layer, this band considerably overlaps with the N(*2p*) band, partly mixed with the U(*5f*) states (similar effects occur with the O_2 molecule atop the surface U atom [P2]). In contrary, the O(*2p*) band remains quasi-isolated from the other bands (analogously to the O atom incorporated into the N vacancy in UN bulk [82]). Position of the N(*2p*) band is insensitive to presence of O atoms and lies within energy range of -6 and -1 eV.

9.2.6. *Comparison of oxygen incorporation into N vacancy on the UN(001) and (110) surfaces*

Similarly to results for perfect UN surface as well as vacancy formation and atomic oxygen adsorbtion, it could be interesting further to compare incorporation (E_I) and solution (E_S) energies for two surfaces, *i.e.* UN (001) and (110) (Fig. 9.6). Table 9.2 compares these energies as function of slab thickness and supercell size. One can see that the UN(110) surface is characterized by more negative solution energy, eVen though the difference between their solution energies is ~0.3. eV. On the other hand, the incorporation energy changes this trend suggesting more negative values for the (001) surface. Moreover, the difference between incorporation energies approaches to 0.4 eV. Such results demonstrate importance of E_I calculations as our surface might function under extreme conditions like high temperatures. Nevertheless, we clearly see similar tendencies for both surfaces (Table 9.2).

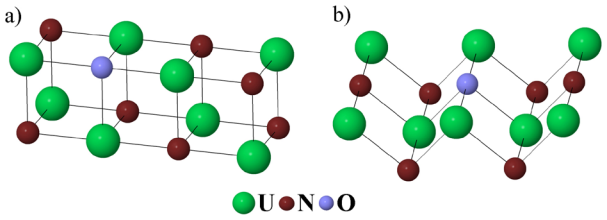

Figure 9.6. 2-layer models of oxygen incorporation into surface N vacancy on UN (001) (a) and (110) (b) surface

Table 9.2. Incorporation (E_I) and solution (E_S) energies, average spin magnetic moments of U atoms and effective charge on O atoms for oxygen incorporated into N vacancy on UN (001) and (110) surfaces. The reference states for calculations on the incorporation and solution energies are the chemical potentials of O and N calculated for O_2 and N_2 molecules, respectively (2 × 2 and 3 × 3 supercells).

Number of layers and supercell size	E_I (eV)	E_S (eV)	μ_{av}^{U} (μ_B)	q_{eff}(e^-)	E_I (eV)	E_S (eV)	μ_{av}^{U} (μ_B)	q_{eff}(e^-)
	(001) surface				(110) surface			
5, 2 × 2	-6.173	-2.473	1.647	-1.36	-5.853	-2.778	1.736	-1.27
7, 2 × 2	-6.181	-2.476	1.495	-1.36	-5.822	-2.794	1.516	-1.29
9, 2 × 2	-6.186	-2.479	1.412	-1.36	-5.820	-2.784	1.472	-1.29
11, 2 × 2	-6.195	-2.483	1.365	-1.35	-5.817	-2.791	1.416	-1.29
7, 3 × 3	-6.126	-2.480	1.463	-1.36	-5.748	-2.783	1.471	-1.28

9.2.7. Modeling of O adatom incorporation: summary

Considerable energetic preference of O atom incorporation into the N vacancy as compared to U vacancy indicates that the observed oxidation of UN is determined mainly by the interaction of oxygen atoms with the surface and sub-surface N vacancies.

The formation of oxynitrides [18] near the UN(001) surface is proposed, which can be caused by diffusion of the oxygen atoms within the interlayers of uranium nitride with further capture by nitrogen vacancies, thus, resulting in their stabilization due to formation of the chemical bonds with the nearest uranium atoms. The electronic charge redistributions demonstrate quite local nature of the density perturbation caused by the incorporated O atoms. The analysis of density of states shows both overlapping of the O(2*p*) states with the N(2*p*) states at initial stages of oxidation (*surface incorporation*) and separation of the O(2*p*) states from other bands in the case of deeper positioned oxygen atoms (*sub-surface penetration*). The results of this analysis could be used for the interpretation of the experimental ultraviolet photoelectron spectra for uranium oxynitrides [18].

10. Summary

The PAW method is used to analyze basic UN bulk properties, point defects behavior on UN surface as well as oxygen interaction with UN surface. We obtain results of such calculations for pure UN bulk an surface, nitride and uranium vacancies on the surface, atomic and molecular adsorbtion as well as oxygen diffusion on UN(001) surface which hase been performed with complete relaxation. We estimate surface supercell size and slab thickness which allow us to obtain accurate results for UN surface. It has been found that use of 7-layer slab with 3×3 surface extension vectors gives results that are qualitatively close to single defect model. However, in the case of smaller 2×2 supercells and 5-layers slabs one can observe noticeable lateral interaction between the defects. We have also compared energies of (*i*) nitrogen vacancy formation, (*ii*) oxygen atom adsorption upon U or N surface atom as well (*iii*) O atom incorporation into N vacancy evaluated for both UN (001) and (110) surfaces.

In spite of aforesaid, some questions about UN surface are still opened. evaluations of formation energies for U vacancies performed so far demand additional verifications of these results using other theoretical methods as well as further development of uranium atom pseudopotentials. To obtain more precise results for oxygen diffusion along the UN(001) surface, the Nudged Elastic Band method [49] must be applied which allows one to obtain more realistic trajectories of atom migration. The performance of this approach will be significantly improved when using the latest release of *VASP-5* computer code as compared to *VASP-4* version used for calculations within this PhD Thesis. It will allow us to obtain reasonable results during the reasonable CPU time. The new experimental measuruments on UN surface (for example, EXAFS measurments, which allow one to observe atomic environment around separate atoms or UPS spectra for identification of oxynitride-like structures) will be also significant for versatile pucture construction of UN oxidation process. This is also important for elaboration of reliable protection of UN samples against aggressive influence of oxygen.

On the whole, the results described in the PhD Thesis represent the significant step for modeling of actinide compounds and promote to better understanding of UN surface oxidation.

11. Main theses

- The results obtained using the two substantially different DFT computational methods based on formalisms of Plane-Waves (PW) and Linear Combination of Atomc Orbitals (LCAO) demonstrate their good qualitative agreement, *i.e.* serve as a reliable verification of obtained results.
- The formation energies for U and N vacancies indicate a clear trend for segregation of vacancies towards the surface (and probably, grain boundaries).
- Results obtained for interaction of O atoms and O_2 molecules with UN surfaces demonstrate a strong chemisorption, typical for metallic adsorbents. The possibility for spontaneous dissociation of the adsorbed oxygen molecules upon the perfect UN(001) surface, analogously to the O_2 dissociation on metallic surfaces, has been demonstrated. After molecular dissociation, O adatom forms a strong chemical bond with the U_{surf} atom beneath which can be considered as one-center surface complex. In the case of O adatom positioned atop the N_{surf} atom, this complex is rather multi-center which involves 4 adjacent U_{surf} atoms.
- High mobility of O_{ads} atoms along the surface due to relatively low migration barriers (<0.5 eV) has been demonstrated. The possibility of low-barrier (~0.5-1 eV) oxygen adatom incorporation into existing N vacancy from the nearest adsorption site atop U_{surf} atom has been proved too as well as energetical stability of UN surface containing incorporated oxygen atoms.
- The following stages for reactivity of oxygen positioned atop the UN surface could be suggested: (*i*) chemisorption of molecular oxygen, (*ii*) spontaneous breaking of the O_2 chemical bond after molecular adsorption, (*iii*) location of the two newly formed O adatoms atop the adjacent surface U atoms, (*iv*) high mobility of O_{ads} atoms along the surface, (*v*) low-barrier incorporation of oxygen adatoms from the positions atop U_{surf} atoms into the nearest N vacancies, *(vi)* stabilization of O_{ads} atom inside N_{surf} vacancy, (*vii*) incorporation of O atoms in existing subsurface N vacancies as a result of inter-lattice diffusion. This explains an easy UN oxidation observed in air.

12. Literature

12.1. Author's publications related to this work

[P1] R.A. Evarestov, A.V. Bandura, M.V. Losev, E.A. Kotomin, Yu.F. Zhukovskii, and D. Bocharov, A first principles DFT study in UN bulk and (001) surface: Comparative LCAO and PW calculations. - J. Comput. Chem., 2008, **29**, p. 2079-2087.

[P2] Yu.F. Zhukovskii, D. Bocharov, E.A. Kotomin, R.A. Evarestov, and A.V. Bandura, First principles calculations of oxygen adsorption on the UN(001) surface. - Surf. Sci., 2009, **603**, p. 50-53.

[P3] Yu.F. Zhukovskii, D. Bocharov, and E.A. Kotomin, Chemisorption of a molecular oxygen on the UN(001) surface: *ab initio* calculations. - J. Nucl. Mater., 2009, **393**, p. 504-507.

[P4] D. Bocharov, D. Gryaznov, Yu.F. Zhukovskii, and E.A. Kotomin, DFT calculations of point defects on UN(001) surface. - Surf. Sci., 2011, **605**, p. 396-400.

[P5] D. Bocharov, D. Gryaznov, Yu.F. Zhukovskii, E.A. Kotomin, *Ab initio* modeling of oxygen impurity atom incorporation into uranium mononitride surface and subsurface vacancies. - J. Nucl. Mater., 2011, **416,** p. 200-204.

12.2. Other author's publications

[O1] D. Bocharov, A. Kuzmin, J. Purans, and Yu.F. Zhukovskii, Quantum chemistry studies of the O *K*-edge X-ray absorption in WO_3 and AWO_3. - SPIE Proceedings, 2008, 71420T (p. 1-9).

[O2] N. Zaporina, O. Doynikova, A. Krumina, D. Bocharov, and J. Grabis, Methods of electron microdiffraction and X-ray analysis in structure study of nanodisperse partially stabilized ZrO_2 powders. - J. Surf. Investigation: X-ray, Synchrotron and Neutron Techniques, 2009, **3**, p. 464-467.

[O3] N. Zaporina, J. Grabis, V.N. Timofeev, and D. Bocharov**,** Microstructural investigations of multicomponent SiC/Si_3N_4-Al_2O_3-Y_2O_3 nanopowders. - Latv. J. Chem., 2010, No 1, p. 33-38.

12.3. References

[1] Hj. Matzke, Science of Advanced LMFBR Fuel, North Holland, Amsterdam, 1986.

[2] The Nuclear Fuel Cycle. P.D. Wilson (Eds.), University Press, Oxford, 1996.

[3] H. Wiame, M. Centeno, S. Pacard, P. Bastian, and P. Grange, Thermal oxidation under oxygen of zirconium nitride studied by XPS, DRIFTS, TG-MS. - J. Eur. Ceram. Soc., 1998, **18**, p. 1293-1299.

[4] M. Walter, Oxidation of inert matrices, JRC-ITU-TN-2005/35 (Research report).

[5] N. Curry, An investigation of the magnetic structure of uranium nitride by neutron diffraction. - Proc. Phys. Soc., 1965, **86**, p. 1193-1198.

[6] T. Muromura and H. Tagawa, Lattice parameter of uranium mononitride. - J. Nucl. Mater., 1979, **79**, p. 264-266.

[7] P.E. Evans and T.J. Davies, Uranium nitrides. - J. Nucl. Mater., 1963, **10**, p. 43-55.

[8] N.-T.H. Kim-Ngan, A.G. Balogh, L. Havela, and T. Gouder, Ion beam mixing in uranium nitride thin films studied by Rutherford Backscattering Spectroscopy. - Nucl. Instr. Meth. Phys. Res. B, 2010, **268**, p. 1875–1879.

[9] G.W. Chinthaka Silva, Ch.B. Yeamans, L. Ma, G.S. Cerefice, K.R. Czerwinski, and A.P. Sattelberger, Microscopic characterization of uranium nitrides synthesized by oxidative ammonolysis of uranium tetrafluoride. - Chem. Mat., 2008, **20**, p. 3076-3084.

[10] G.C. Allen and N.R. Holmes, The passivation of uranium metal surfaces by nitrogen bombardment - the formation of uranium nitride. - J. Nucl. Mater., 1988, **152**, p. 187-193.

[11] P.R. Norton, R.L. Tapping, D.K. Creber, and W.J.L. Buyers, Nature of the 5*f* electrons in uranium nitride: A photoelectron spectroscopic study of UN, U, UO_2, ThN, and Th. - Phys. Rev. B, 1980, **21**, p. 2572-2577.

[12] T. Ito, H. Kumigashira, S. Souma, T. Tahakashi, and T. Suzuki, High-resolution angle-resolved photoemission study of UN and USb; Dual character of 5*f* electrons. - J. Magn. Magn. Mater., 2001, **226-230**, p. 68-69.

[13] M. Marutzky, U. Barkow, J. Schoenes, and R. Troć, Optical and magneto-optical properties of single crystalline uranium nitride. - J. Magn. Magn. Mater., 2006, **299**, p. 225–230.

[14] B. Reihl, G. Hollinger, and F.J. Himpsel, Itinerant 5*f*-electron antiferromagnetism in uranium nitride: A temperature-dependent angle-resolved photoemission study. - Phys. Rev. B, 1983, **28**, p. 1490–1494.

[15] M. Paljević and Z. Despotović, Oxidation of uranium mononitride. - J. Nucl. Mater., 1975, **57**, p. 253-257.

[16] Y. Arai, M. Morihira, and T. Ohmichi, The effect of oxygen impurity on the characteristics of uranium and uranium-plutonium mixed nitride fuels. - J. Nucl. Mater., 1993, **202**, p. 70-78.

[17] L. Black, F. Miserque, T. Gouder, L. Havela, J. Rebizant, and F. Wastin, Preparation and photoelectron spectroscopy study of UN_x thin films. - J. Alloys Comp., 2001, **315**, p. 36–41.

[18] M. Eckle, and T. Gouder, Photoemission study of UN_xO_y and UC_xO_y in thin films. - J. Alloys Comp., 2004, **374**, p. 261–264.

[19] S. Sunder and N.H. Miller, XPS and XRD studies of corrosion of uranium nitride by water. - J. Alloys Comp., 1998, **271–273**, p. 568–572.

[20] D. Sedmidubsky, R.J.M. Konings, and P. Novak, Calculation of enthalpies of formation of actinide nitrides. - J. Nucl. Mater., 2005, **344**, p. 40–44.

[21] P. Weinberger, C.P. Mallett, R. Podloucky, and A. Neckel, The electronic structure of HfN, TaN and UN. - J. Phys. C: Solid St. Phys., **13**, 1980, p. 173-187.

[22] M.S. Brooks and D. Glötzel, Some aspects of the electronic structure of uranium pnictides and chalcogenides. - Physica B, 1980, **102**, p. 51-58.

[23] M.S. Brooks, Electronic structure of NaCl-type compounds of the light actinides. I. UN, UC, and UO. - J. Phys. F: Met. Phys., 1984, **14**, 639-652.

[24] G.K. Johnson and E.H.P. Cordfunke, The enthalpies of formation of uranium mononitride and α- and β-uranium sesquinitride by fluorine bomb calorimetry. - J. Chem. Thermodyn., 1981, **13**, p. 273-282.

[25] R. Atta-Fynn and A.K. Ray, Density functional study of the actinide nitrides. - Phys. Rev. B, 2007, **76**, 115101 (p. 1-12).

[26] P.F. Weck, E. Kim, N. Balakrishnan, F. Poineau, C.B. Yeamans, and K.R. Czerwinski, First-principles study of single-crystal uranium mono- and dinitride. - Chem. Phys. Lett., 2007, **443**, p. 82–86.

[27] Y. Lu, B.-T. Wang, R.-W. Li, H. Shi, and P. Zhang, Structural, electronic, and thermodynamic properties of UN: Systematic density functional calculations. - J. Nucl. Mater., 2010, **406,** p. 218–222.

[28] B. Dorado, B. Amadon, M. Freyss, and M. Bertolus, DFT+*U* calculations of the ground state and metastable states of uranium dioxide. - Phys. Rev. B, 2010, **79**, 235125 (p. 1-8)

[29] B. Dorado, G. Jomard, M. Freyss, and M. Bertolus, Stability of oxygen point defects in UO_2 by first-principles DFT+*U* calculations: Occupation matrix control and Jahn-Teller distortion. - Phys. Rev. B, 2010, **82**, 035114 (p. 1-11).

[30] D. Gryaznov, E. Heifets and E.A. Kotomin, *Ab initio* DFT+*U* study of He atom incorporation into UO_2 crystals. - Phys. Chem. & Chem. Phys., 2009, **11**, p. 7241-7247

[31] D. Rafaja, L. Havela, R. Kuel, F. Wastin, E. Colineau, and T. Gouder, Real structure and magnetic properties of UN thin films. – 2005, **386,** p. 87-95.

[32] Z. Yongbin, M. Daqiao, Z. Zhenghe, and M. Meizhong, Pseudopotential plane-wave study of the uranium metals and uranium compounds. – Chin. J. Chem. Phys., 2005, **18**, p. 735-739.

[33] E.A. Kotomin, Yu.A. Mastrikov, Yu.F. Zhukovskii, P. Van Uffelen, and V.V. Rondinella, First-principles modelling of defects in advanced nuclear fuels. - Phys. Stat. Sol. (c), 2007, **4**, p. 1193-1196.

[34] E.A. Kotomin, R.W. Grimes, Yu.A. Mastrikov, and N.J. Ashley, Atomic scale DFT simulations of point defects in uranium nitride. - J. Phys.: Cond. Mat, 2007, **19**, 106208 (p. 1-9).

[35] E.A. Kotomin, D. Gryaznov, R.W. Grimes, D. Parfitt, Yu.F. Zhukovskii, Yu.A. Mastrikov, P. Van Uffelen, V.V. Rondinella, and R.J.M. Konings, First-principles modelling of radiation defects in advanced nuclear fuels. - Nucl. Instr. Meth. Phys. Res. B, 2008, **266**, p. 2671–2675.

[36] R.A. Evarestov, M.V. Losev, A.I. Panin, N.S. Mosyagin, and A.V. Titov, Electronic structure of crystalline uranium nitride: LCAO DFT calculations. - Phys. Stat. Solidi (b), 2008, **245**, p. 114 -122.

[37] R.A. Evarestov, A.I. Panin, A.V. Bandura, and M.V. Losev, Electronic structure of crystalline uranium nitrides UN, U_2N_3 and UN_2: LCAO calculations with the basis set optimization. – J. Phys.: Conf. Ser., 2008, **117**, 012015 (p. 1-8).

[38] K.N. Kudin, G. E. Scuseria, and R.L. Martin, Hybrid Density-Functional Theory and the insulating gap of UO_2. - Phys. Rev. Lett. 2002, **89**, 266402 (p. 1-4).

[39] S.L. Dudarev, G.A. Botton, S.Y. Savrasov, C.J. Humphreys, and A.P. Sutton, Electron-energy-loss spectra and the structural stability of nickel oxide: An LSDA+*U* study. - Phys. Rev. B, 1998, **57**, p. 1505–1509.

[40] F. Gupta, G. Brillant, and A. Pasturel, Correlation effects and energetics of point defects in uranium dioxide: a first principle investigation. - Phil. Mag., 2007, **87**, p. 2561–2569.

[41] M. Freyss, First-principles study of uranium carbide: Accommodation of point defects and of helium, xenon, and oxygen impurities. - Phys. Rev. B, 2010, **81**, 014101 (p. 1-16).

[42] H. Shibata, T. Tsuru, M. Hirata, and Y. Kaji, First principles study on elastic properties and phase transition of NpN - J. Nucl. Mater., 2010, **401**, p. 113–117.

[43] C.D. Taylor, Evaluation of first-principles techniques for obtaining materials parameters of α-uranium and the (001) α-uranium surface. - Phys. Rev. B, 2008, **77**, 094119 (p. 1-9).

[44] P.E. Bloechl, Projector augmented-wave method. - Phys. Rev. B, 1994, **50**, p. 17953-17979.

[45] A.H.H. Tan, M. Abramowski, R.W. Grimes, and S. Owens, Surface defect configurations on the (100) dipolar surface of UO_2. - Phys. Rev. B, 2005, **72,** p. 035457 (p. 1-6).

[46] F.N. Skomurski, R.C. Ewing, A.L. Rohl, J.D. Gale, and U. Becker, Quantum mechanical *vs.* empirical potential modeling of uranium dioxide (UO_2) surfaces: (111), (110), and (100). - Amer. Mineral., 2006, **91,** p. 1761-1772.

[47] M.N. Huda and A.K. Ray, Electronic structures and bonding of oxygen on plutonium layers. - Eur. Phys. J. B, 2004, **40**, p. 337–346.

[48] R. Atta-Fynn and A. K. Ray, *Ab initio* full-potential fully relativistic study of atomic carbon, nitrogen, and oxygen chemisorption on the (111) surface of δ-Pu. - Phys. Rev. B, 2007, **75**, 195112 (p. 1-13).

[49] G. Kresse and J. Furthmüller, *VASP* the Guide, University of Vienna, 2009; *http://cms.mpi.univie.ac.at/vasp/*

[50] А.В. Бандура и Р.А. Эварестов, Неэмпирические расчеты кристаллов в атомном базисе. Изд-во С.-Петерб. ун-та, Санкт Петербург, 2004 (In Russian).

[51] R.A. Evarestov, Quantum Chemistry of Solids: The LCAO First Principles Treatment of Crystals. Springer Series in Solid State Science, Springer-Verlag, Berlin, 2007.

[52] J. Hafner, *Ab initio* simulations of materials using *VASP*: Density-Functional Theory and beyond. - J. Comput. Chem., 2008, **29**, p. 2044–2078.

[53] L.N. Kantorovich, Quantum Theory of the Solid State: an Introduction. Springer-Verlag, Berlin, 2004.

[54] J.P. Perdew, J.A. Chevary, S.H. Vosko, K.A. Jackson, M.R. Pederson, D.J. Singh, and C. Fiolhais, -Phys. Rev. B, 1992, **46**, p. 6671–6687.

[55] A. Unsöld, Beiträge zur Quantenmechanik des Atoms. - Ann. Phys., 1927, **82**, p. 355-393 (In German); *http://demonstrations.wolfram.com/UnsoeldsTheorem/*

[56] M. Krack, Pseudopotentials for H to Kr optimized for gradient-corrected exchange-correlation functionals. - Theor. Chem. Acc., 2005, **114**, p. 145-152.

[57] N.W. Ashcroft and N.D. Mermin, Solid State Physics. Saunders College Press, Philadelphia, 1976.

[58] G. Kresse and D. Joubert, From ultrasoft pseudopotentials to the projector augmented-wave method. - Phys. Rev. B, 1999, **59**, p. 1758-1775.

[59] H.J. Monkhorst and J.D. Pack, Special points for Brillouin-zone integrations. - Phys. Rev. B, 1976, **13**, p. 5188-5192.

[60] M. Methfessel and A.T. Paxton, High-precision sampling for Brillouin-zone integration in metals. - Phys. Rev. B, 1989, **40**, p. 3616–3621.

[61] G. Kresse and J. Furthmüller, Efficient iterative schemes for *ab initio* total-energy calculations using a plane-wave basis set. - Phys. Rev. B, 1996. **54**, p. 11169-11186.

[62] A. Stathopoulos and C.F. Fischer, A Davidson program for finding a few selected extreme eigenpairs of a large, sparse, real, symmetric matrix. - Comput. Phys. Comm., 1994, **79**, p. 268–290.

[63] R. Dovesi, V.R. Saunders, C. Roetti, R. Orlando, C.M. Zicovich-Wilson, F. Pascale, B. Civalleri, K. Doll, N.M. Harrison, I.J. Bush, Ph. D'Arco and M. Llunell, *CRYSTAL*2006 User's Manual, Università di Torino, Turin, 2006; *http://www.crystal.unito.it/*

[64] J.P. Perdew, K. Burke, and M. Ernzerhof, Generalized gradient approximation made simple. - Phys. Rev. Lett., 1996, **77**, p. 3865-3868.

[65] S. Piskunov, E. Heifets, R.I. Eglitis, and G. Borstel, Bulk properties of $SrTiO_3$, $BaTiO_3$ and $PbTiO_3$ perovskites: An *ab initio* HF/DFT study. - Comput. Mater. Sci., 2004, **29**, p. 165-178.

[66] M.J. Frisch, J.A. Pople, and J.S. Binkley, Self-consistent molecular orbital methods 25. Supplementary functions for Gaussian basis sets. - J. Chem. Phys., 1984, **80**, p. 3265-3269.

[67] W. Kuchle, M. Dolg, H. Stoll, and H. Preuss, Energy-adjusted pseudopotentials for the actinides. Parameter sets and test calculations for thorium and thorium monoxide. - J. Chem. Phys., 1994, **100**, p. 7535- 7544.

[68] A.V. Titov and N.S. Mosyagin, Generalized relativistic effective core potential: Theoretical grounds. - Int. J. Quant. Chem., 1999, 71, p. 359–401.

[69] G. Gilat, General analytic method of zone integration for joint densities of states in metals. - Phys. Rev. B, 1982, **26**, p. 2243–2246.

[70] P.W. Tasker, The stability of ionic crystal surfaces. - J. Phys. C: Solid State Phys., 1979, **12**, p. 4977-4984.

[71] A. Subramanian, L.D. Marks, O. Warschkow, and D.E. Ellis, Direct observation of charge transfer at a MgO (111) surface. - Phys. Rev. Lett., 2004, **92**, 026101 (p. 1-4).

[72] J. Akella, S. Weir, J. M. Wills, and P. Söderlind, Structural stability in uranium. - J. Phys.: Condens. Matter, 1997, **9**, L549 (p. 1-7).

[73] C.G. Van de Walle and J. Neugebauer, First-principles calculations for defects and impurities: Applications to III-nitrides. - J. Appl. Phys., 2004, **95**, p. 3851-3879.

[74] P. Söderlind, First-principles elastic and structural properties of uranium metal. - Phys. Rev. B, 2002, **66.** 085113 (p. 1-7).

[75] B. Dorado, M. Freyss, and G. Martin, GGA+*U* study of the incorporation of iodine in uranium dioxide. - Eur. Phys. J. B, 2009, **69,** p. 203-210.

[76] D.R. Lide (ed.), CRC Handbook of Chemistry and Physics, 88th Edition, CRC Press (2007-2008).

[77] M. Iwasawa, Y. Chen, Y. Kaneta, T. Ohnuma, H. Y. Geng, and M. Kinoshita, First-principles calculation of point defects in uranium dioxide. - *Mat. Trans*, 2006, **47,** p. 2651-2657.

[78] NIST Chemistry Web-book (2010); *http://www.webbook.nist.gov/chemistry/*

[79] Yu.F. Zhukovskii, P.W.M. Jacobs, and M. Causà, On the mechanism of the interaction between oxygen and close-packed single-crystal aluminum surfaces. - J. Phys. Chem. Solids, 2003, **64**, p. 1317-1331.

[80] S. Piskunov, Yu.F. Zhukovskii, E.A. Kotomin, E. Heifets, and D.E. Ellis, Adsorption of atomic and molecular oxygen on the $SrTiO_3$(001) surfaces: Predictions by means of hybrid density functional calculations. - MRS Proc., 2006, **894**, LL08-05 (p. 1-6).

[81] R. Weast, CRC Handbook of Chemistry and Physics. CRC Press Inc., Boca Baton (FL), 1985.

[82] E.A. Kotomin and Yu.A. Mastrikov, First-principles modelling of oxygen impurities in UN nuclear fuels. - J. Nucl. Mater., 2008, **377**, p. 492-495.

[83] R.W. Grimes and C.R.A. Catlow, The stability of fission products in uranium dioxide. - Phil. Trans. Roy. Soc. A, 1991, **335**, p. 609-634.

[84] Y.-L. Lee, J. Kleis, J. Rossmeisl, and D. Morgan, *Ab initio* energetics of $LaBO_3$ (001) (B = Mn, Fe, Co, and Ni) for solid oxide fuel cell cathodes. - Phys. Rev. B, 2009, **80**, 224101 (p. 1-20).

[85] Yu.A. Mastrikov, R. Merkle, E. Heifets, E.A. Kotomin, and J. Maier, Pathways for oxygen incorporation in mixed conducting perovskites: a DFT-based mechanistic analysis for (La, Sr)$MnO_{3-\delta}$. - J. Phys. Chem. C, 2010, **114**, p. 3017-3027.

13. Contributions at scientific conferences

1. ***23rd ISSP Conference (Riga, Latvia, February, 2007).*** D. Bocharov, Yu.F. Zhukovskii, and E.A. Kotomin, "First-principles simulations of oxygen adsorption on perfect and defective UN(001) surface". Abstracts: p. 17.
2. ***The 5th International Conference "Information Technologies and Management", IT&M'2007 (Riga, Latvia, April, 2007).*** Yu.F. Zhukovskii, D. Bocharov, and E.A. Kotomin, "Oxygen chemisorption on the UN(001) surface: periodic DFT simulation". Abstracts: p. 9-10.
3. ***24th Institute of Solid State Physics Conference (Riga, Latvia, February, 2008).*** D. Bocharov, Yu.F. Zhukovskii, D. Gryaznov, R.A. Evarestov, and E.A. Kotomin, "Structure and properties of UN nuclear fuels: quantum chemistry approach". Abstracts: p. 6.
4. ***International Baltic Sea Region conference "Functional materials and nanotechnologies 2008" (Riga, Latvia, April, 2008).*** D. Bocharov, Yu. Zhukovskii, R.A. Evarestov, E.A. Kotomin, and A. Bandura, "Atomic and molecular oxygen adsorption on the UN(001) surface". Abstracts: p. 87.
5. ***7th International Workshop "Materials Models and Simulations for Nuclear Fuels" (Karlsruhe, Germany, September, 2008).*** D. Bocharov, Yu.F. Zhukovskii, and E.A. Kotomin, "Interaction of the oxygen molecule with the UN(001) surface: *Ab initio* modeling".
6. ***25th ISSP Conference (Riga, Latvia, February, 2009).*** D. Bocharov, Yu.F. Zhukovskii, and E.A. Kotomin, "Chemisorption of a molecular oxygen on the UN(001) surface". Abstracts: p. 54.
7. ***International conference "Functional materials and nanotechnologies" FM&NT-2009 (Riga, Latvia, April, 2009).*** D. Bocharov, D. Gryaznov, Yu.F. Zhukovskii, and E.A. Kotomin, "Perfect and defective (001) surface of uranium nitride: *ab initio* calculations". Abstracts: p. 100.
8. ***The 7th International Conference "Information Technologies and Management", IT&M'2009 (Riga, Latvia, April, 2009).*** D. Bocharov, D. Gryaznov, Yu.F. Zhukovskii, and E.A. Kotomin, "*Ab initio* calculations on the atomic and electronic structure of defective UN(001) surface". Abstracts: p. 32-33.
9. ***International Workshop "DFT modelling of actinide solid solutions with the emphasis to bulk properties and Helium behaviour" (Karlsruhe, Germany, September, 2009).*** Yu.F. Zhukovskii, E.A. Kotomin, D. Bocharov, and V.N. Kuzovkov, "The DFT+U calculations on defects in PuO_2 and MOX".
10. ***26th ISSP Conference (Riga, Latvia, February, 2010).*** D. Bocharov, D. Gryaznov, Yu.F. Zhukovskii and E.A. Kotomin, "Surface and subsurface vacancies in uranium nitride: first principles calculations". Abstracts: p. 31.
11. ***International conference "Functional materials and nanotechnologies" FM&NT-2010 (Riga, Latvia, March, 2010).*** D. Bocharov, D. Gryaznov, Yu.F. Zhukovskii and E.A. Kotomin, "First principles calculations on oxygen impurities incorporated in the vacancies of UN(001) substrate". Abstracts: p. 37.
12. ***The 8th International Conference "Information Technologies and Management", IT&M'2010 (Riga, Latvia, April, 2010).*** D. Bocharov, D. Gryaznov, Yu.F. Zhukovskii, and E.A. Kotomin, "*Ab initio* calculations on pure and oxygen-occupied vacancies upon the UN(001) surface". Abstracts: p. 38-39.

13. ***Spring European Materials Research Society (E-MRS) Meeting (Strasbourg, France, June, 2010).*** D. Bocharov, D. Gryaznov, Yu.F. Zhukovskii, and E.A. Kotomin, „Ab initio modeling of oxygen impurities incorporated within UN(001) surface and subsurface vacancies". Abstracts: NPVI-23.
14. ***F-BRIDGE School on Ceramic Nuclear Fuel and Cladding Materials (Karlsruhe, Germany, September-October, 2010).*** D. Bocharov, D. Gryaznov, Yu.F. Zhukovskii, and E.A. Kotomin, "First principles calculations of surface and subsurface vacancies as well as oxygen impurity atoms on UN(001) substrate".
15. ***27th ISSP Conference (Riga, Latvia, February, 2011).*** D. Bocharov, Yu.F. Zhukovskii, D. Gryaznov, and E.A. Kotomin, "Oxygen diffusion processes on UN(001) surface". Abstracts: p. 23.
16. ***45th Russian School on Condensed State Physics (St. Petersburg, Russia, March, 2011).*** D. Bocharov, D. Gryaznov, Yu.F. Zhukovskii, and E.A. Kotomin, „Quantum-chemical modeling of oxidation processes on surface of nitride nuclear fuel". Abstracts: p. 27.
17. ***International conference "Functional materials and nanotechnologies" FM&NT-2011 (Riga, Latvia, April, 2011).*** Yu.F. Zhukovskii, D. Bocharov, D. Gryaznov, and E.A. Kotomin, "First-principles simulations on initial stage of uranium nitride surface oxidation". Abstracts: p. 20.
18. ***International conference "Functional materials and nanotechnologies" FM&NT-2011 (Riga, Latvia, April, 2011).*** D. Bocharov, Yu.F. Zhukovskii, D. Gryaznov, and E.A. Kotomin, "UN(110) surface properties: ab initio calculations". Abstracts: p. 166.
19. ***Spring European Materials Research Society (E-MRS) Meeting (Nice, France, May, 2011).*** D. Bocharov, Yu.F. Zhukovskii, D. Gryaznov, and E.A. Kotomin, "First-principles simulations on initial stages of UN(001) surface oxidation". Abstracts: V4-17.

Acknowledgements

The author gratefully acknowledges the doctoral studies support by the European Social Fund and European Social Fund project No. 2009/0216/1DP/1.1.1.2.0/09/APIA/VIAA/044. The author sincerely thanks J. Chepkasova, R.A. Evarestov, D. Gryaznov, V. Kashcheyevs, E.A. Kotomin, A. Kuzmin, Yu.A. Mastrikov, P. Nazarov, S. Piskunov, J. Timoshenko, P. Van Uffelen, and G. Zvejnieks for valuable suggestions and many stimulating discussions. The technical assistance of A. Gopejenko and A. Gusev is the most valuable. Special gratitute is expressed to my scientific advisor Yu.F. Zhukovskii for permanent support of scientific work during the whole period of PhD studentship, including Thesis preparation as well as to my teacher of chemistry J. Zaikina, teacher of physics M. Samucevicha and to my parents.